J. Fluid Mech. (2012), *vol.* 710, *pp.* 453–481.
doi:10.1017/jfm.2012.373

Geometry and interaction of structures in homogeneous isotropic turbulence

T. Leung, N. Swaminathan† and P. A. Davidson

Department of Engineering, University of Cambridge, Trumpington Street, Cambridge CB2 1PZ, UK

(Received 17 August 2011; revised 23 May 2012; accepted 19 July 2012;
first published online 29 August 2012)

A strategy to extract turbulence structures from direct numerical simulation (DNS) data is described along with a systematic analysis of geometry and spatial distribution of the educed structures. A DNS dataset of decaying homogeneous isotropic turbulence at Reynolds number $Re_\lambda = 141$ is considered. A bandpass filtering procedure is shown to be effective in extracting enstrophy and dissipation structures with their smallest scales matching the filter width, L. The geometry of these educed structures is characterized and classified through the use of two non-dimensional quantities, 'planarity' and 'filamentarity', obtained using the Minkowski functionals. The planarity increases gradually by a small amount as L is decreased, and its narrow variation suggests a nearly circular cross-section for the educed structures. The filamentarity increases significantly as L decreases demonstrating that the educed structures become progressively more tubular. An analysis of the preferential alignment between the filtered strain and vorticity fields reveals that vortical structures of a given scale L are most likely to align with the largest extensional strain at a scale 3–5 times larger than L. This is consistent with the classical energy cascade picture, in which vortices of a given scale are stretched by and absorb energy from structures of a somewhat larger scale. The spatial distribution of the educed structures shows that the enstrophy structures at the 5η scale (where η is the Kolmogorov scale) are more concentrated near the ones that are 3–5 times larger, which gives further support to the classical picture. Finally, it is shown by analysing the volume fraction of the educed enstrophy structures that there is a tendency for them to cluster around a larger structure or clusters of larger structures.

Key words: isotropic turbulence structure, turbulent flows

1. Introduction

Kolmogorov's universal theory of small scales is of pre-eminent importance for homogeneous turbulence. While it successfully describes the lower-order statistics, it fails to capture the higher-order statistics of the small scales. It has been observed in numerous studies that the small scales are highly intermittent, occupy a small region of the flow, appear to form coherent structures and lead to the non-Gaussian statistics of the velocity increments. Understanding their geometry and spatial arrangement is therefore key in completing the picture of small-scale turbulence.

Siggia (1981) showed that an intense vorticity field consists of long thin tubular structures, and later studies (Hosokawa & Yamamoto 1990; She, Jackson & Orszag 1991; Vincent & Meneguzzi 1991; Jiménez *et al.* 1993, for example) at higher

† Email address for correspondence: ns341@cam.ac.uk

Reynolds number ($Re_\lambda > 100$) further demonstrated that such a field is organized as vortex filaments. The width of these filaments is typically of the order of a few dissipation scales, and their length of the order of the integral scale. Jiménez *et al.* (1993) proposed scaling laws for these filaments, and concluded that these structures only account for a small volume fraction of the entire flow. Furthermore, their circulation Reynolds number increases with $Re_\lambda^{1/2}$. Given the rather small kinetic energy content of these worm-like structures, one might wonder about their significance in the overall dynamics of turbulence and their exact role in the energy cascade. This has led to some interest in the role of vortex sheets (Ruetsch & Maxey 1994) in the energy cascade, suggesting that worm-like structures are generated by a one-step sheet roll-up process caused by Kelvin–Helmholtz instability (Vincent & Meneguzzi 1994). These vortex sheets are in turn produced by pancake-like structures that become flattened over time. This picture is different from the classical Richardson's cascade picture. Vincent & Meneguzzi (1994) also attributed the merging of several small parallel vortex tubes into a larger structure as an example of energy backscatter. The dynamics of strained vortex sheets also suggests that vortex tubes will eventually be formed by the disintegration of sheets if the intense vorticity accumulates within them (Passot *et al.* 1995). Goto & Kida (2003) and Goto (2008) investigated the role of the strain field created by anti-parallel tubular vortex pairs in stretching smaller vortices as per the classical picture. However, a mechanism for the formation of the anti-parallel tubes was not identified.

The inherent difficulty in identifying turbulent eddies, which are not simple geometrical objects such as sheets, ribbons, tubes or spheres, creates a major challenge in studying the structure of homogeneous turbulence. Early studies (She *et al.* 1991) relying on vector field visualization concluded that low-magnitude vorticity regions are not organized and are of no particular geometry, while intense vorticity regions are organized as filaments. Various point-based quantitative measures have been proposed in past studies (Hunt, Wray & Moin 1988; Jeong & Hussain 1995). Such schemes identify whether the local points of interest in the flow belong to a vortex or not, with an emphasis on vortex tubes. These methods have also been refined to identify the vortex core and sheet (Horiuti 2001; Horiuti & Takagi 2005). Nevertheless, these point-based schemes do not provide information on the geometrical characteristics of an entire structure.

There are recent studies that aim at identifying individual structures of either filtered or unfiltered enstrophy or dissipation fields as connected isosurfaces, after which the geometry of these educed structures can be observed and classified. Moisy & Jimenez (2004) observed that moderate and intense vorticity structures are respectively ribbon- and tube-like, moderate strain field structures are mostly complex without any distinct shape, while the intense strain field structures appear to be ribbon- and sheet-like. They followed a fractal approach to analyse the geometry of the connected isosurfaces obtained after thresholding the vorticity and strain fields. Bermejo-Moreno & Pullin (2008) and Bermejo-Moreno, Pullin & Horiuti (2009) further explored this strategy by employing the curvelet transform to the enstrophy and dissipation fields to separate structures of a given scale of interest before identifying connected isosurfaces at a chosen thresholding value. However, instead of the fractal approach, the principal curvatures of the identified structures were used to construct the *differential-geometry* properties such as shape index and curvedness. Since these two quantities are local on the isosurface, their joint probability density function (p.d.f.) was used to obtain appropriate moments of the shape index, $\hat{S}$, and curvedness, $\hat{C}$. These two moments

along with another dimensionless parameter, known as the stretching parameter constructed using the volume enclosed by the isosurface and its surface area, SP, were then used as signatures of the educed structure in a three-dimensional $(\hat{S}, \hat{C}, SP)$ visualization space. This analysis technique was applied to homogeneous isotropic turbulence to study the geometry of the enstrophy and dissipation structures (Bermejo-Moreno & Pullin 2008) and their proximities (Bermejo-Moreno *et al.* 2009). Their results show a continuous evolution from blobs to tubes to highly stretched sheets as one moves down in scale, and also support the view that on average dissipation or strain rate structures are more planar than the enstrophy structures. These techniques have also been explored to study Lagrangian structures in homogeneous (Yang, Pullin & Bermejo-Moreno 2010) and inhomogeneous (Yang & Pullin 2011) turbulent flows.

The persistence of tubes in homogeneous turbulence has puzzled many researchers. In his classical work, Betchov (1956) predicted that the strain field in isotropic turbulence is biaxial on average, and has one strong compressive and two weaker extensional strain rates. Such a strain field might favour the formation of sheet-like structures, but sheets are seldom seen. The preferential alignment between vorticity and strain has been the focus of many studies in the past to shed more light on the role of straining motion in the energy cascade. While one would expect the vorticity to be aligned with the largest extensional strain for the most effective stretching, evidence of the vorticity aligning with the intermediate strain is overwhelming (Ashurst *et al.* 1987; She *et al.* 1991; Vincent & Meneguzzi 1994; Horiuti 2001, for example), and some theoretical explanation using local and non-local effects of the strain field has been given (Jiménez 1992; Nomura & Post 1998; Hamlington, Schumacher & Dahm 2008).

Aside from the geometry of these multi-scale structures, their spatial distribution and organization is also important in the description of small-scale dynamics. Early works described the inertial range as a random distribution of coherent structures uniformly distributed in space (Townsend 1951; Tennekes 1968). However, recent numerical experiments show that 'worms' have a strong tendency to cluster, and the clustering of intense vorticity in the inertial range is shown by Moisy & Jimenez (2004) using the box-counting technique. In addition, the clustering of fine-scale structures on the periphery of larger structures has been observed experimentally by Worth (2010). The proximity of enstrophy structures at different scales has also been examined by Bermejo-Moreno *et al.* (2009).

The objective of this study is to shed more light on the structure of enstrophy and dissipation fields in homogeneous isotropic turbulence, as well as their roles in the energy cascade and clustering. These three objectives are achieved by first educing these structures using a multi-scale extraction algorithm, which is a bandpass filtering procedure described in § 2. While intermediate steps such as using a threshold value and isosurfacing are common, this extraction algorithm and the geometry description technique used in this study are different from the methodology and technique used by Bermejo-Moreno & Pullin (2008). In this study, a bandpass filter, simpler than the curvelet transform technique, is used to educe structures which are then visualized using an isosurface for a given threshold. The morphology of these educed structures is characterized using geometrical descriptors constructed from the Minkowski functionals, which have roots in *integral-geometry* and aim to describe the global aspects of a structure in terms of its characteristic thickness, width and length with a minimal amount of subjectivity. The three characteristic dimensions lead to the construction of two simple non-dimensional measures called 'filamentarity' and 'planarity' as described in § 3, which are convenient geometrical descriptors of

the structures identified in this study. These analysis techniques are then used to address the primary objectives: the alignment of these educed structures, their spatial distributions, and their roles in the energy cascade and clustering. These are discussed respectively in §§ 4 and 5, and the conclusions of this study are summarized in § 6.

2. Structure identification scheme

2.1. *Bandpass filtering*

An extraction algorithm allowing vortical structures at different scales to be identified is needed as the first step of this study. Simple thresholding of the vorticity field often does not produce the desired result as small intense structures tend to mask the low-amplitude structures. However, by first applying a bandpass filter to the velocity or vorticity field, structures that do not match the filter scale L can be suppressed allowing the dominant structures associated with L to be observed. In this study, the velocity field is filtered, from which the filtered vorticity and strain fields are constructed since the operations of differentiation and filtering commute. To begin this procedure, it is necessary to define the low-pass filtered velocity field,

$$\boldsymbol{u}^L(\boldsymbol{x}) = \int \boldsymbol{u}(\boldsymbol{x}-\boldsymbol{r})G(L;r)\,\mathrm{d}\boldsymbol{r}, \tag{2.1}$$

where $\boldsymbol{u}^L(\boldsymbol{x})$ is the velocity field filtered at the scale L, $G(L;r)$ is the filter function, and $r=|\boldsymbol{r}|$. The simplest filter that is both spherically symmetric and reasonably compact in physical space is the Gaussian filter, defined as

$$G(L;r) = \frac{1}{\pi^{3/2}L^3}\exp\left(-\frac{r^2}{L^2}\right), \quad \int G(L;r)\,\mathrm{d}\boldsymbol{r} = 1. \tag{2.2}$$

The filtered field, $\boldsymbol{u}^L(\boldsymbol{x})$, contains predominantly information about scales greater than L, and so $L(\partial\boldsymbol{u}^L/\partial L)$ should contain information centred around the scale L. Hence, we define the bandpass filtered velocity field as

$$\boldsymbol{u}_b^L = -\frac{\alpha L}{\sqrt{L}}\frac{\partial \boldsymbol{u}^L}{\partial L}, \tag{2.3}$$

where α is a dimensionless coefficient to be defined shortly. Following the convolution theorem, the low-pass filtered velocity field has the Fourier transform

$$\widehat{\boldsymbol{u}}^L(\boldsymbol{k}) = T(\kappa)\widehat{\boldsymbol{u}}(\boldsymbol{k}), \quad T(\kappa) = 8\pi^3\widehat{G}(\boldsymbol{k}). \tag{2.4}$$

Here $\boldsymbol{k}$ is the wavenumber vector, and $\kappa = kL/2$ with $k=|\boldsymbol{k}|$. The transfer function for a Gaussian filter is $T(\kappa)=\exp(-\kappa^2)$. The transform of the bandpass filtered velocity field is then

$$\widehat{\boldsymbol{u}}_b^L = -\frac{\alpha\kappa}{\sqrt{L}}\frac{\mathrm{d}T}{\mathrm{d}\kappa}\widehat{\boldsymbol{u}}(\boldsymbol{k}). \tag{2.5}$$

Furthermore, it is convenient to introduce

$$T_b(\kappa) = -\kappa\frac{\mathrm{d}T}{\mathrm{d}\kappa} = 2\kappa^2\exp(-\kappa^2), \tag{2.6}$$

from which

$$\widehat{\boldsymbol{u}}_b^L = \frac{\alpha}{\sqrt{L}}T_b(\kappa)\widehat{\boldsymbol{u}}(\boldsymbol{k}). \tag{2.7}$$

Combining (2.5) and (2.6), the bandpass filtered energy spectrum can be written as

$$E_b^L(L;k) = \frac{\alpha^2}{L} T_b^2(\kappa) E(k), \tag{2.8}$$

where E_b^L and $E(k)$ represent the energy spectra of the filtered, $\boldsymbol{u}_b^L(\boldsymbol{x})$, and the unfiltered, $\boldsymbol{u}(\boldsymbol{x})$, velocity fields respectively. Finally the normalization coefficient α is chosen such that the following relationship is satisfied:

$$\int_0^\infty E_b^L(L;k)\,\mathrm{d}L = E(k). \tag{2.9}$$

This requires

$$\alpha^2 \int_0^\infty \frac{T_b^2(\kappa)}{\kappa}\,\mathrm{d}\kappa = 1, \tag{2.10}$$

and the resulting value of α for a Gaussian filter is therefore $\sqrt{2}$.

The effectiveness of this filtering method for educing structures of different scales is demonstrated in the Appendix using some examples. The important points can be summarized as follows. The bandpass filter attenuates eddies of sizes $\ell \gg Ł$ and $\ell \ll Ł$; however, the filtered field contains traces of eddies ranging from L to $4L$ with a maximum at $\ell = \sqrt{5}L$ in the case of a spherical eddy. The filter is sharper for $\ell < L$ and less so for $\ell > L$. There is also a small dilatation of eddies, which is most significant for $\ell < L$. Since these eddies are effectively damped by the filter, this dilatation effect should not be important. For $\ell > L$, the dilatation is less significant. For structures with more than one length scale, the filter predominantly educes those whose smallest length scale matches the filter width L.

2.2. *Filtering scalar fields from a DNS database*

The bandpass filter described in § 2.1 is applied to a decaying homogeneous isotropic turbulence simulated using direct numerical simulation (DNS). The details of this simulation can be found in Tanahashi, Miyauchi & Ikeda (1999). The incompressible Navier–Stokes equations were solved using the Fourier spectral method in a cubic domain of size 2π with 400 grid points in each direction. This dataset has $Re_\lambda = 141$ and velocity derivative $(\partial u/\partial x)$ skewness of about -0.53, which signifies that the turbulence is fully developed. The ratio of the computational domain size to the integral length scale, ℓ, is 3.77. The Taylor microscale, λ, and the Kolmogorov scale, η, are related to ℓ by the ratio of $\ell/\lambda = 8.33$ and $\ell/\eta = 200$ respectively. The numerical resolution in this simulation is $k_{max}\eta \sim 1.5$.

Filtered scalar fields, such as enstrophy, $\omega_i\omega_i$, and dissipation, $S_{ij}S_{ij}$, can be constructed from the filtered velocity field $\boldsymbol{u}_b^L$. The filter scales L used in this analysis are given in table 1 along with some relevant statistics of the filtered fields. The fraction of turbulent kinetic energy in each of these scales compared to the unfiltered mean value shows the expected behaviour of a decrease in $\overline{|\boldsymbol{u}_b^L|^2}$ as the filter scale decreases. On the other hand, the mean, standard deviation, and maximum values of the filtered enstrophy and dissipation fields increase as the filter scale decreases, which is also expected.

The turbulent kinetic energy spectra constructed using the unfiltered and filtered fields are shown in figure 1. A threshold has to be applied to the filtered scalar fields so that individual structures can be identified as connected isosurfaces. The expectation

ID	Scale, L	$\frac{\overline{\lvert \boldsymbol{u}_b^L \rvert^2}}{\overline{\lvert \boldsymbol{u} \rvert^2}}$	Enstrophy $\frac{m_L}{m_o}$	Enstrophy $\frac{s_L}{s_o}$	Enstrophy $\frac{\max_L}{\max_o}$	Dissipation $\frac{m_L}{m_o}$	Dissipation $\frac{s_L}{s_o}$	Dissipation $\frac{\max_L}{\max_o}$
F1	$0.75\ell(150\eta)$	0.356	0.0036	0.0018	0.0002	0.0037	0.0020	0.0003
F2	$0.50\ell(100\eta)$	0.270	0.0080	0.0040	0.0006	0.0080	0.0047	0.0009
F3	$0.25\ell(50\eta)$	0.114	0.0245	0.0133	0.0021	0.0245	0.0151	0.0034
F4	$\lambda(24\eta)$	0.043	0.0847	0.0511	0.0159	0.0847	0.0566	0.0191
F5	15η	0.024	0.1875	0.1215	0.0423	0.1831	0.1324	0.0589
F6	10η	0.013	0.3238	0.2292	0.1127	0.3162	0.2427	0.1448
F7	5η	0.004	0.5120	0.4647	0.2506	0.5002	0.4728	0.3602

TABLE 1. Filter settings used in the DNS data analysis and the corresponding mean, m, standard deviation, s, and maximum values. The subscripts L and o respectively denote values associated with the filtered at scale L and unfiltered fields.

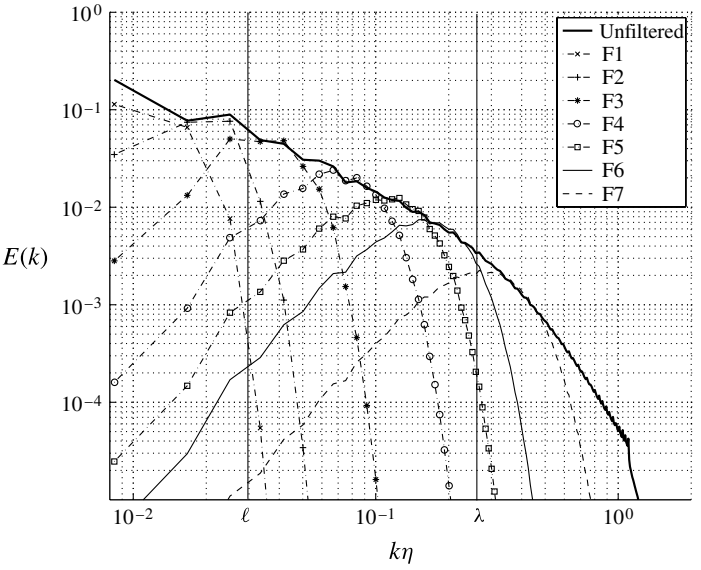

FIGURE 1. Bandpass filtered energy spectra.

that increasing the threshold value would result in structures that are less volume-filling and more sparse has been verified by comparing educed structures obtained using different threshold values. For a given filter scale, often several structures obtained using a high threshold are enclosed by one large structure obtained using a lower threshold. Despite a variation in the volume of these structures, their general shape and spatial distribution are not drastically altered by varying the threshold. In the present study, a value of $m_L + 1.5s_L$ is chosen as the threshold for all the filtered fields given in table 1 unless stated otherwise. The kinetic energy content of these educed structures obtained after thresholding is $\sim$10 % of the total in the bandpass filtered field.

The typical structures identified by thresholding the filtered enstrophy fields are shown in figure 2(*a–c*) for filters F2–F4 given in table 1. As the filter scale decreases,

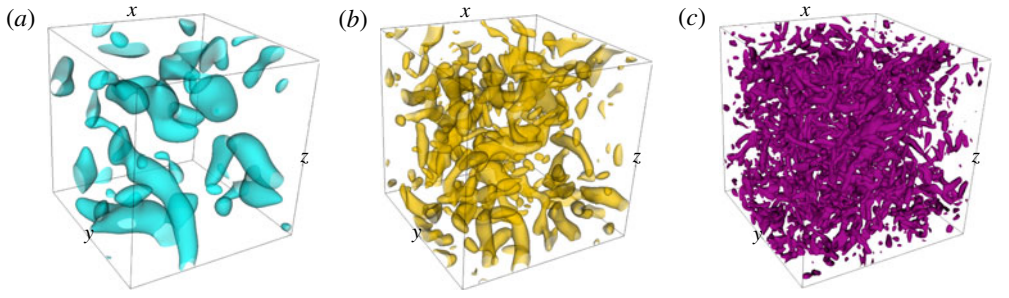

FIGURE 2. (Colour online) Bandpass filtered enstrophy fields for filters F2–F4 in table 1: (*a*) $L_2 = 0.50\ell$ (100η); (*b*) $L_3 = 0.25\ell$ (50η); (*c*) $L_4 = \lambda$ (24η).

the structures become increasingly difficult to discern when visualizing the entire domain. Therefore, for a closer examination of the small scales, the filtered enstrophy fields for F3, F4, F6 and F7 are shown within a thin slice of the domain with dimensions of $2\pi \times 2\pi \times 3\lambda$ (or 72η) in figure 3. The fine-scale structures at $L_6 = 10\eta$ and $L_7 = 5\eta$ certainly appear to be worm-like. The two intermediate filter settings $L_3 = 0.25\ell$ or 50η and $L_4 = \lambda$ or 24η also give tubular structures. As the filter scale increases, the structures tend to be more blob-like than tube-like. There is some suggestion in figure 3 that the small worms are concentrated at the periphery of larger structures, a point to be noted for discussion in § 5. The larger structures appear to be quite 'empty'. As Goto (2008) noted earlier, it is generally untrue that a large-scale structure encompasses a cluster of smaller vortices. There are also some fine-scale structures that are found relatively far away from the larger ones. One possible explanation is that they can be the debris of dissipating structures.

The filtered estrophy and dissipation fields for the filter F6 are compared in figure 4. The dimensions of the domain shown in this figure are $2\pi \times 2\pi \times 3\lambda$ (or 72η) as in figure 3. When the two fields are superimposed (figure 4*c*), they closely mirror each other; however, detailed structural features of these two fields are quite different. One qualitative observation is that the dissipation field is more fragmented and irregular than the enstrophy field at the small scale. The dissipation structures, which appear to be shorter and flatter, seldom overlap the relatively more worm-like enstrophy structures. Often a long worm-like enstrophy structure is in close contact with or is sandwiched between a few smaller dissipation structures. This observation is consistent with the view that fine-scale structures are similar to Burgers vortices, because the intense dissipation region in a Burgers vortex does not coincide with its intense enstrophy region. However, the regions of high strain do not form an annulus around the high enstrophy regions, which would be the case for a single Burgers vortex.

3. Morphology of turbulence structures

3.1. *Minkowski functionals and shapefinders*

In addition to the visual examination of the filtered scalar fields, a less subjective and more robust method is needed to obtain a statistical description of the morphology of turbulence structures. As noted in § 1, visualization quantities and schemes based on local point-based information have been attempted in many past studies. Moreover, properties of the principal curvatures (κ_1, κ_2) have also been used to represent the 'non-local' geometry of turbulence structures (Bermejo-Moreno & Pullin 2008;

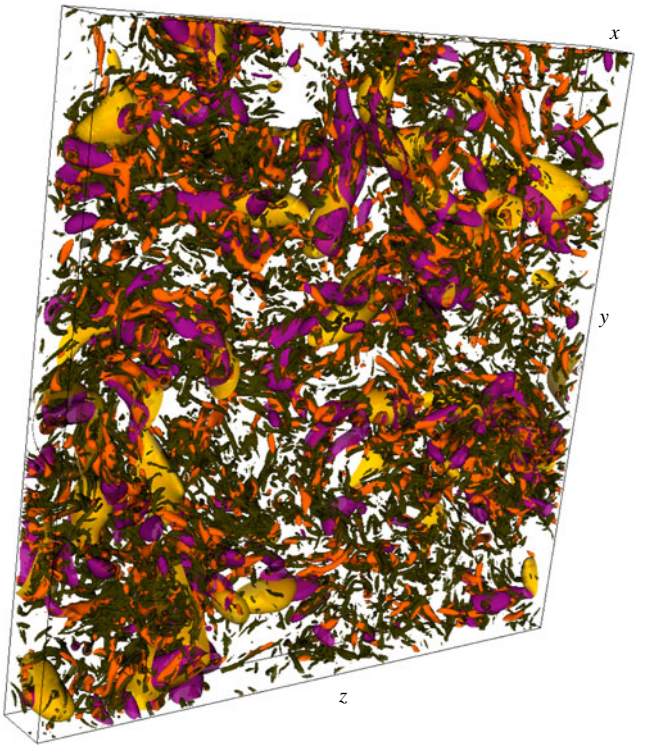

FIGURE 3. Typical picture of the filtered enstrophy fields in a subdomain of size $2\pi \times 2\pi \times 3\lambda(=72\eta)$. Four filter settings, see table 1, are shown: yellow – F3, purple – F4, orange – F6 and dark green – F7.

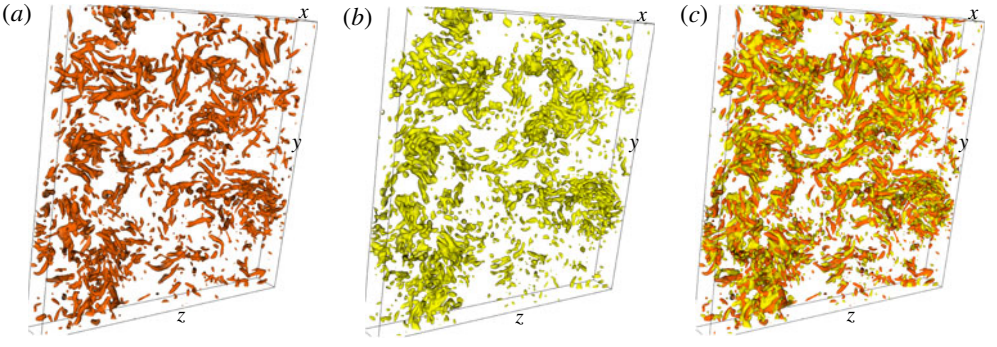

FIGURE 4. Filtered (*a*) enstrophy, (*b*) dissipation and (*c*) superimposed fields for F6 in table 1 ($L_6 = 10\eta$).

Bermejo-Moreno *et al.* 2009). The topological quantities such as the genus or the Euler characteristic, related to the Gaussian curvature integrated over the surface of a structure, are effective descriptors of the global aspects of a structure as noted by Mecke, Buchert & Wagner (1994). However, these are not adequate for the full morphological identification of spatial structures in a multi-scale problem

such as turbulence. This issue has been recognized in cosmology while attempting to describe the geometry and topology of galaxies and their superclusters (see for example Mecke *et al.* 1994 and references therein), which led to the use of Galilean invariant morphological properties called the *Minkowski functionals* from integral-geometry. Hadwiger's theorem (Hadwiger 1957) states that there are $d+1$ Minkowski functionals in d-dimensional space, and thus for a three-dimensional space there are four functionals. They are given by Sahni, Sathyaprakash & Shandarin (1998) and Einasto *et al.* (2007):

$$V_0 = V, \quad V_1 = \frac{S}{6}, \quad V_2 = \frac{1}{3\pi}\int_S \frac{\kappa_1+\kappa_2}{2}\,\mathrm{d}S, \quad V_3 = \frac{1}{2\pi}\int_S (\kappa_1\kappa_2)\,\mathrm{d}S. \tag{3.1}$$

The first two functionals are related to the volume, V, and surface area, S, of a three-dimensional object. The latter two, V_2 and V_3, are related to the integrated mean and Gaussian curvatures respectively. The functional V_3 is also a topological invariant known as the Euler characteristic and is often denoted as χ. These functionals have been used extensively to quantify the morphology of complex cosmological structures (Mecke *et al.* 1994; Kerscher *et al.* 1997; Schmalzing & Buchert 1997; Sahni *et al.* 1998; Schmalzing *et al.* 1999; Sheth, Shandarin & Sathyaprakash 2003; Shandarin, Sheth & Sahni 2004; Sheth & Sahni 2005; Einasto *et al.* 2007) as well as the structure of the magnetic field in a small-scale dynamo (Wilkin, Barenghi & Shukurov 2007). To the knowledge of the present authors, this method has not been applied to describe the morphology of turbulence structures. Although one of the objectives in this study (identification and classification of turbulence structures) is similar to that of Bermejo-Moreno & Pullin (2008), the details of these two studies are different. As noted in § 1, Bermejo-Moreno & Pullin (2008) used curvelet transforms and differential-geometry descriptors, whereas this study employs bandpass filtering and Minkowski functionals based on integral-geometry giving an effective global descriptor. Furthermore, there is an important difference in the findings of these two studies, as will be noted later.

Using the the Minkowski functionals in (3.1), Sahni *et al.* (1998) proposed three *shapefinders*: thickness, $\mathscr{T}$, width, $\mathscr{W}$, and length, $\mathscr{L}$, as follows:

$$\mathscr{T} = \frac{V_0}{2V_1}, \quad \mathscr{W} = \frac{2V_1}{\pi V_2}, \quad \mathscr{L} = \frac{3V_2}{2V_3}. \tag{3.2}$$

These shapefinders have dimension of length and they are positive semi-definite quantities for convex objects. This can explain why we do not have many negative shapefinders despite the presence of partial concavity in many structures. The isoperimetric inequalities for the Minkowski functionals resulting from the Alexandrov–Fenchel inequality give $\mathscr{T} \leqslant \mathscr{W} \leqslant \mathscr{L}$ for convex bodies (Schmalzing *et al.* 1999). It is easy to verify that in the special case of a sphere of radius $\mathscr{R}$, $\mathscr{T} = \mathscr{W} = \mathscr{L} = \mathscr{R}$. For an infinitely long cylinder with radius $\mathscr{R}_1$, these shapefinders yield $\mathscr{T} = 1.5\mathscr{R}_1$ and $\mathscr{W} = 2\mathscr{R}_1$. Thus, the shapefinders strictly give representative scales for the spatial extent of a structure, and do not return its exact dimensions except for the sphere. However, these shapefinders scale very well with the three principal axes of a triaxial ellipsoid (Sahni *et al.* 1998).

While the above inequality and non-negativeness apply for convex shapes, there is a possibility that one of the local principal curvatures may be negative, representing a locally concave surface as in saddles (see Bermejo-Moreno & Pullin 2008 for illustration of such surfaces). However, a joint probability density function of the two principal curvatures (not shown in this paper) for enstrophy structures educed at various scales suggests that the probability of finding negative curvature locally

is very small in the present filtered data. This is consistent with the observations of Bermejo-Moreno & Pullin (2008), and suggests that the entities of our interest are typically made of convex surfaces in an integral sense, thus ensuring that $V_3 \geqslant 0$. Although in general V_3 can be positive, negative or zero, for a closed surface we have $\chi = V_3 = 2$. This is the only case observed in the present analysis since no structure with holes (multiply connected structures) was found in the filtered datasets at the threshold values of $m + 1.5s$ used. It should be noted that lowering the threshold value can yield multiply connected structures and care is required to obtain $\mathscr{L}$ as noted below. However, lowering the threshold to $m + 0.5s$ gives structures with holes of $\sim 5\,\%$ or less of the extracted structures. Thus, one can conclude that the multiply connected structures are insignificant for this study.

We note that care is required with the interpretation of V_3 when holes are present in the structure because V_3 can become zero or negative (Sheth & Sahni 2005). For these situations, $\mathscr{L}$ is defined as $\mathscr{L} = 3V_2/4(G + 1)$, where $G = 1 - V_3/2$ is the genus of the structure (Sheth *et al.* 2003). The genus is defined as the number of cuts that can be made along a simple curve on an object without splitting it. Thus with every additional hole, G increases by 1. For example, $G = 0$ for a closed surface, $G = 1$ for a torus, and $G = 2$ for a pretzel. Therefore, for $G > 0$, $\mathscr{L}$ represents the characteristic length between two holes. One can also verify that $\mathscr{L}$, as given above, scales with the ring radius of a circular torus, which has $G = 1$. Despite these more extensive definitions, one must note that bandpass filtering will inevitably 'smudge' the details of the structures such as small holes in a sheet. As a result, $V_3 = 2$ in our filtered datasets, and hence definitions (3.1) and (3.2) are adequate for our purposes.

Representing the three parameters in (3.2) in dimensionless form, two quantities called the planarity, $\mathscr{P}$, and filamentarity, $\mathscr{F}$, can be defined (Sahni *et al.* 1998) as

$$\mathscr{P} = \frac{\mathscr{W} - \mathscr{T}}{\mathscr{W} + \mathscr{T}}, \quad \mathscr{F} = \frac{\mathscr{L} - \mathscr{W}}{\mathscr{L} + \mathscr{W}}. \tag{3.3}$$

These two dimensionless quantities are bounded such that $0 \leqslant \mathscr{P} \leqslant 1$ and $0 \leqslant \mathscr{F} \leqslant 1$ when $\mathscr{T} \leqslant \mathscr{W} \leqslant \mathscr{L}$ is satisfied. As noted earlier, $\mathscr{T} = \mathscr{W} = \mathscr{L}$ for a perfect sphere yielding $(\mathscr{P}, \mathscr{F}) = (0, 0)$. A filament is characterized by one large dimension, $\mathscr{L}$, compared to the other two dimensions, $\mathscr{W}$ and $\mathscr{T}$, implying that an infinitely long tube would have $\mathscr{F} = 1$ since $\mathscr{L} \gg \mathscr{W}$. The value of $\mathscr{P}$ would then depend on the cross-section of such a filament, where a large value of $\mathscr{P}$ would indicate the shape of a ribbon for $\mathscr{W} \gg \mathscr{T}$, and a small value of $\mathscr{P}$ would indicate a round tube for $\mathscr{W} \sim \mathscr{T}$. On the other hand, a very thin sheet would have one very small dimension ($\mathscr{T}$), so that $\mathscr{P} = 1$ represents a sheet with negligible thickness. In the case of a sheet, a large value of $\mathscr{F}$ would indicate a pancake that is stretched out more in one direction, resembling an infinitely long ribbon. If $\mathscr{F} \sim 0$, then the shape resembles a circular thin sheet. Thus, the three quantities $\mathscr{T}, \mathscr{W}$ and $\mathscr{L}$ expressed in dimensionless form as $\mathscr{P}$ and $\mathscr{F}$ provide a relatively simple and intuitive way to describe the shapes of various three-dimensional objects. In order to further illustrate the geometry represented by $\mathscr{P}$ and $\mathscr{F}$, a simple schematic is provided in figure 5. The four special cases $(\mathscr{P}, \mathscr{F}) = (0, 0)$, (0, 1), (1, 0) and (1, 1) as described above are labelled in the schematic, as well as regions roughly corresponding to other common shapes.

We shall examine the morphology derived from the above scheme for typical turbulence structures. By way of illustration, a number of individual enstrophy structures educed from the filtered field using the filter F3 are shown in figure 6. The corresponding shapefinders $(\mathscr{P}, \mathscr{F})$ for these structures are also given. Figure 6(*a*)

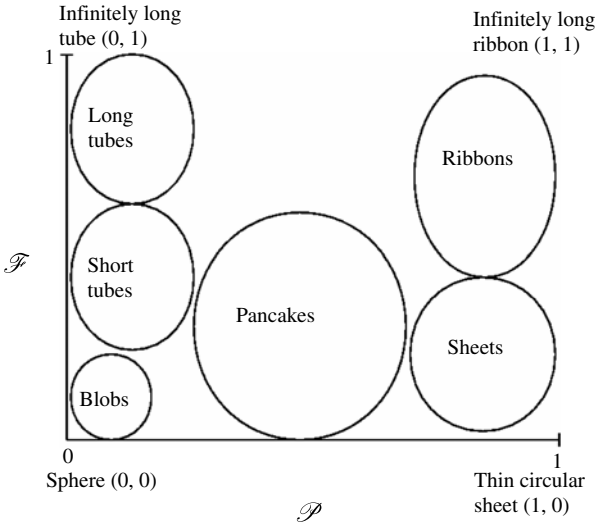

FIGURE 5. Typical regions for various simple shapes in the $\mathscr{P}$–$\mathscr{F}$, shapefinders, plane.

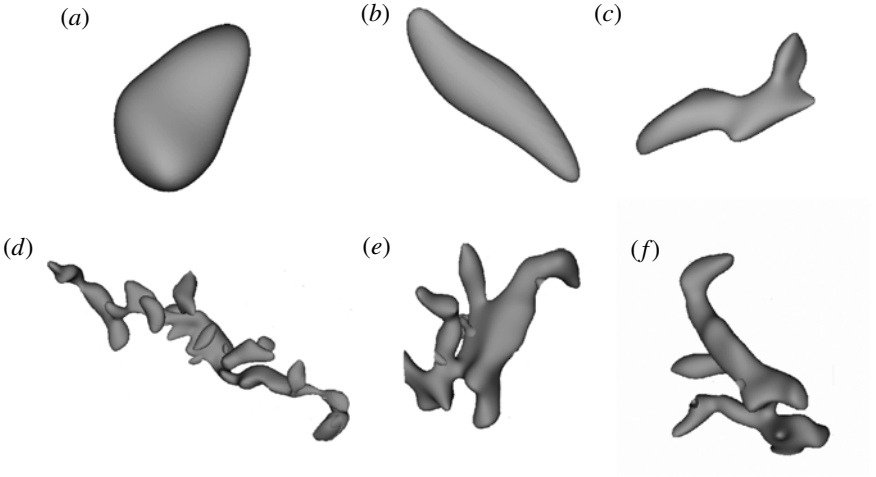

FIGURE 6. Sample structures extracted from the DNS and their shapefinders, $(\mathscr{P}, \mathscr{F})$, in the enstrophy field filtered using the F3 filter: (*a*) $(\mathscr{P}, \mathscr{F}) = (0.044, 0.066)$; (*b*) (0.0885, 0.269); (*c*) (0.107, 0.431); (*d*) (0.085, 0.850); (*e*) (0.010, 0.808); (*f*) alternative view of (*e*).

shows an irregular shape but a relatively simple blob-like structure. Its shape can be characterized by its $\mathscr{P}$ and $\mathscr{F}$, and both are less than 0.1. Figure 6(*b*) shows a short tube, which has a small $\mathscr{P}$ but a larger $\mathscr{F}$. Figure 6(*c*) is a more complex shape with a twisted surface containing some local negative curvatures. It still has a small $\mathscr{P}$ and a large $\mathscr{F}$, and can be characterized as a short tube. Two more complex structures are shown in figure 6(*d,e*). Both of these structures, whether appearing like a single convoluted worm (figure 6*d*) or with several branches (shown as two alternative views in figure 6*e,f*), would be classified as long tubular structures with a similar signature of $(\mathscr{P}, \mathscr{F})$. The long worm-like structure in figure 6(*d*) has a higher $\mathscr{P}$ value than

that in figure 6(*e*), which indicates that on average its shape is more planar. Since both $\mathscr{P}$ values are very small, it is difficult to distinguish the differences in planarity with the naked eye.

It can be seen that the general shape of very complex structures can be captured by the present scheme. The presence of saddle points and bends on the surface (i.e. negative principal curvatures) does not affect the capability of this scheme to identify the general shape of the structure as noted earlier. This is due to the additive property of the Minkowski functionals (Thompson 1996; Michielsen & Raedt 2001). A smooth complex and partially concave object can be closely modelled by joining a group of small convex bodies in the cases observed in this study. For a partially concave body formed by joining two convex bodies, say A and B, the additivity property implies that the Minkowski functional V_i can be approximated as:

$$V_i(A \cup B) = V_i(A) + V_i(B) - V_i(A \cap B). \tag{3.4}$$

In other words, each Minkowski functional of a large partially concave object can be obtained by summing the Minkowski functional of each smaller convex body and then subtracting the value corresponding to the overlapping region. Therefore $\mathscr{L}$, which scales with V_2, for a partially concave body can be closely approximated by summing $\mathscr{L}$ of all the small convex bodies that can be fitted within the larger object. There will be some discrepancies between the 'true length' and $\mathscr{L}$ for any complex structure since there will inevitably be some gaps and/or overlapping parts when modelled using an ensemble of triaxial ellipsoids. Nonetheless, the additivity property of the Minkowski functionals enables this method to be a powerful tool in analysing very complex shapes in the messy world of turbulence.

3.2. *Structures in enstrophy and dissipation fields*

Isosurfaces in the filtered enstrophy and dissipation fields are constructed based on the marching cube algorithm in the visualization software VisIt 2.3.1. Each isosurface is composed of triangulated surface elements and connected elements are counted as one single structure. For each ensemble of educed structures at a given filter scale L, a significant portion of the educed structures are very tiny blobs or fragments that contribute to a negligible part of the total filtered field and are possibly the result of background noise. Therefore structures that are not composed of a sufficient number of surface elements are discarded. Since each structure is defined by triangular surface elements, the discrete numerical scheme proposed by Meyer *et al.* (2002) is used to compute the local principal curvatures κ_1 and κ_2. This discrete scheme can cause some numerical issues when the curvature is very large, which yield negative values for $\mathscr{P}$ and $\mathscr{F}$, which are unphysical. It was found in the analysis that ~6–7 % of the educed structures had negative values, which are excluded from the analysis. Just for the sake of completeness, the negative $\mathscr{P}$ and $\mathscr{F}$ values are shown only in figure 7(*c*). The volume V of each structure is computed by the visualization tool and the surface area S is the sum of the area of all surface elements. The Minkowski functionals and shapefinders can then be obtained for each individual structure using (3.1)–(3.3). The accuracy and robustness of this method to compute the Minkowski functionals are discussed by Sheth *et al.* (2003).

Figure 7 shows the results of geometrical analysis of the enstrophy structures for six different filters, F2–F7 in table 1. The colour (online) of the data points is consistent with the visualizations shown in figure 3. First the dimensional shapefinders $\mathscr{T}$, $\mathscr{W}$ and $\mathscr{L}$, normalized by η, are presented in figure 7(*a,b*). Considering the two smaller

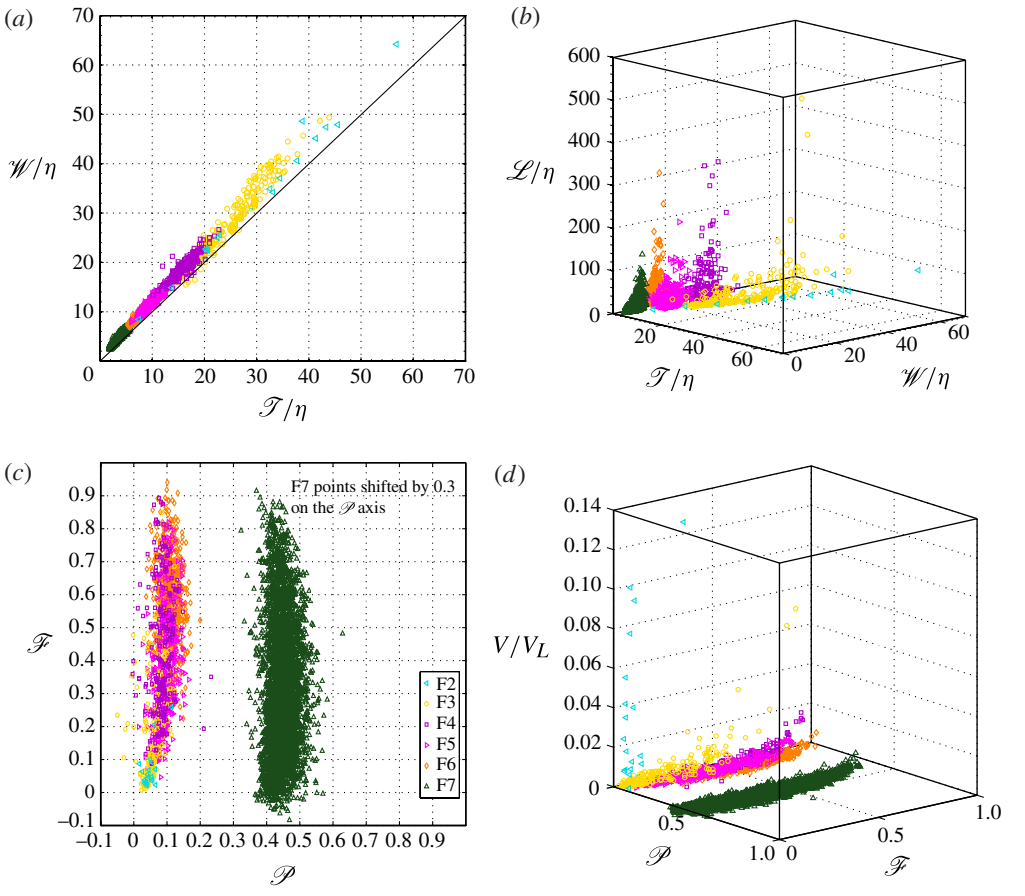

FIGURE 7. (Colour online) Shape analysis of filtered enstrophy structures.

dimensions $\mathscr{T}$ and $\mathscr{W}$ of the structures, the ratio of $\mathscr{T}$ and $\mathscr{W}$ for each group of educed structures produced by a given filter is very similar as suggested by the small spread of the data points of a single symbol in figure 7(*a*). All the data points fall very close to a straight line, which shows a slight skew towards a greater width than thickness. This implies that the majority of the enstrophy structures are mildly flattened with some of them being close to circular. If the educed structures have a circular cross-section, then the data points are expected to lie very close to the diagonal line shown in figure 7(*a*). The data clouds tend to move closer to the diagonal line as the filter scale L decreases. This also shows that no ribbon-like structure ($\mathscr{W} \gg \mathscr{T}$) can be found in the filtered enstrophy fields. The spread in $\mathscr{L}$ is much larger than that in $\mathscr{W}$ and $\mathscr{T}$ for a given filter scale as one can observe in figure 7(*b*). A few structures are significantly longer than others, with the most evident case being F3 ($L = 0.25\ell$ or 50η). The length of the entire computational domain is $\sim 750\eta$, and there are a few F3 structures spanning a sizable portion of the domain. There are still many longer structures from the three smaller filters, particularly F4 and F5, but the difference is less dramatic with decreasing L. On the other hand, the larger filter F2 ($L = 0.50\ell$ or 100η) produced no structure that was markedly longer than others in the same group, indicating some kind of change from F2 to F3.

The dimensionless parameters $\mathscr{P}$ and $\mathscr{F}$ are examined in figure 7(*c*), and additionally the volume fraction V/V_L, defined as the volume of each structure over the total volume of all the structures for a given L, is presented in figure 7(*d*). This additional figure is included because the dimensionless parameters $\mathscr{P}$ and $\mathscr{F}$ do not indicate the relative spatial dominance of these structures. For instance, the entire ensemble of eddies can consist of many small structures of one morphology type that do not occupy a significant portion of the educed total volume, while a handful of dominant structures of a different morphology type account for the majority of the educed total volume. The most notable feature found in the $\mathscr{P}$–$\mathscr{F}$ plot (figure 7*c*) is that $\mathscr{P} < 0.25$ for the vast majority of the enstrophy structures while $\mathscr{F}$ ranges from almost 0 to 0.95. These results suggest that the present structures are mostly tubular or blob-like with no sheet-like (high $\mathscr{P}$) structures found. The greater scatter in $\mathscr{P}$ for 5η (F7) structures is due to a wider range of $\mathscr{W}$ values compared to that of $\mathscr{T}$ values as shown in figure 7(*b*).

Starting at the large filter scale F2, most of the structures can be characterized as blobs with $\mathscr{P}$ and $\mathscr{F}$ values less than 0.1 with a couple of exceptions, but no $\mathscr{F}$ value greater than 0.26 is present. For the F3 structures, it appears that there exist a significant number of blobs whose $\mathscr{P}$ and $\mathscr{F}$ values are small, as well as filaments whose $\mathscr{F}$ values are large. However, a close examination of figure 7(*d*) shows that all blob-like structures with low $\mathscr{P}$ and $\mathscr{F}$ occupy a very small portion of the educed volume for F3 in contrast to the F2 structures. In other words, the ensemble of F3 structures is best characterized by a handful of large dominant tubular structures accompanied by many small blob-like structures. As L decreases, $\mathscr{F}$ increases gradually through F3–F6 while there is also a slight increase in $\mathscr{P}$. This suggests that smaller structures are getting stretched out more in one direction, and are only slightly flattened. Furthermore, the volume distribution becomes more even as L decreases indicating that the finer structures, which are mostly tubular, are of comparable size rather than spatially dominated by a few prominent ones.

To further illustrate the variation in $\mathscr{P}$ and $\mathscr{F}$ with L, the p.d.f.s of $\mathscr{P}$ and $\mathscr{F}$ for filter scales F3–F7 are presented in figures 8(*a*) and 8(*b*) respectively. It is clear that the spread of $\mathscr{P}$ is much smaller than that of $\mathscr{F}$. For decreasing L, $\mathscr{P}$ increases slightly and distinct peaks can be seen in the p.d.f. Since the bandpass filter can educe structures whose smallest length scale matches the filter scale L, the ensemble of structures educed with one filter scale would have a narrow spread of $\mathscr{T}$ (i.e. the smallest dimension). The present analysis shows that most of these structures have close to circular or slightly elliptical cross-sections resulting in a small spread in $\mathscr{P}$. The p.d.f. of $\mathscr{F}$ shows a more continuous distribution rather than distinct peaks, indicating that no characteristic length can be conveniently found for these structures. It has been reported that worm-like structures exist with their diameter of the order of a few Kolmogorov length scales and their length of the order of the integral length scale (Jiménez *et al.* 1993). In this analysis, there are a handful of tubular structures obtained using filters F3–F6 that have $\mathscr{L} \geqslant \ell$. However, the wide spread in $\mathscr{F}$ in figure 7(*c*) shows that the length of these tubular vortices can greatly vary. It is likely that these vortex tubes have an undulating rather than a uniform diameter along their length. Thus their wider portions will appear in a filtered field obtained using a large filter while the narrower portions will appear in that of a smaller filter. A similar observation has been made previously by Jiménez (1994) and Jiménez & Wray (1998). While they observed fine filaments of length $\sim\ell$, such structures are most likely formed by several short and highly strained regions connected by regions of weaker stretching or compression.

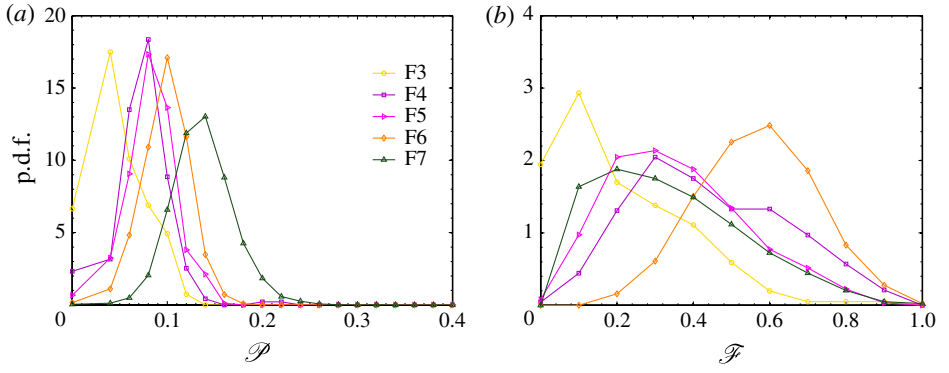

FIGURE 8. (Colour online) p.d.f. of (*a*) planarity, $\mathscr{P}$, and (*b*) filamentarity, $\mathscr{F}$, for enstrophy structures from filters F3 to F7.

The shapefinder values for the enstrophy and dissipation fields filtered using three different filters are compared in figure 9. It is generally believed that the dissipation, $S_{ij}S_{ij}$, structures are more planar. The present analysis does not show that there is a significant increase in $\mathscr{P}$ for these structures. However, they are more numerous and show a slightly wider spread in $\mathscr{P}$ than the enstrophy structures, suggesting that the strain field is more irregular in shape than the vorticity field. This point is further confirmed by the p.d.f. in figure 10. The more varied morphology in the dissipation field suggests that it is more difficult to ascribe a 'typical' shape to the structures present. This is to be expected since there is no strain equivalent of the 'freezing-in' of vortex lines (as per the Helmholtz theorem) at large *Re*.

As noted in § 2.2, a threshold of $m_L + 1.5s_L$ is used to educe structures for this analysis. These analyses have been repeated with $m_L + 2.5s_L$ to study the sensitivity to the choice of the threshold value. The results of $\mathscr{P}$ and $\mathscr{F}$ (not shown) are observed to be very similar to those discussed in this paper, suggesting that these findings are not sensitive to the threshold value.

4. Vorticity and strain field alignment

4.1. *Unfiltered strain field*

The analysis in the previous section supports the dominance of tubular structures, which progressively become more elongated down the scale. This is consistent with the classical picture, in which vortex stretching is presumably the primary mechanism for energy transfer across different scales. However, this idea is seemingly in contradiction with previous studies (Ashurst *et al.* 1987; She *et al.* 1991; Vincent & Meneguzzi 1994, for example), which reported that the most probable alignment of the vorticity was found to be with the intermediate principal strain rate. This is a rather counter-intuitive result as one would expect the largest extensional strain to have the dominant role in stretching vortices if vortex stretching is indeed the primary energy transfer mechanism. Also, the ratio for the three principal strains has been found numerically (Ashurst *et al.* 1987) to be $\lambda_1{:}\lambda_2{:}\lambda_3 = -4{:}1{:}3$. This is consistent with the prediction of Betchov (1956), so the intermediate strain is expected to be mostly small but positive. This favours the presence of biaxial strain and the formation of sheet-like structures, which do not seem to exist in our DNS data.

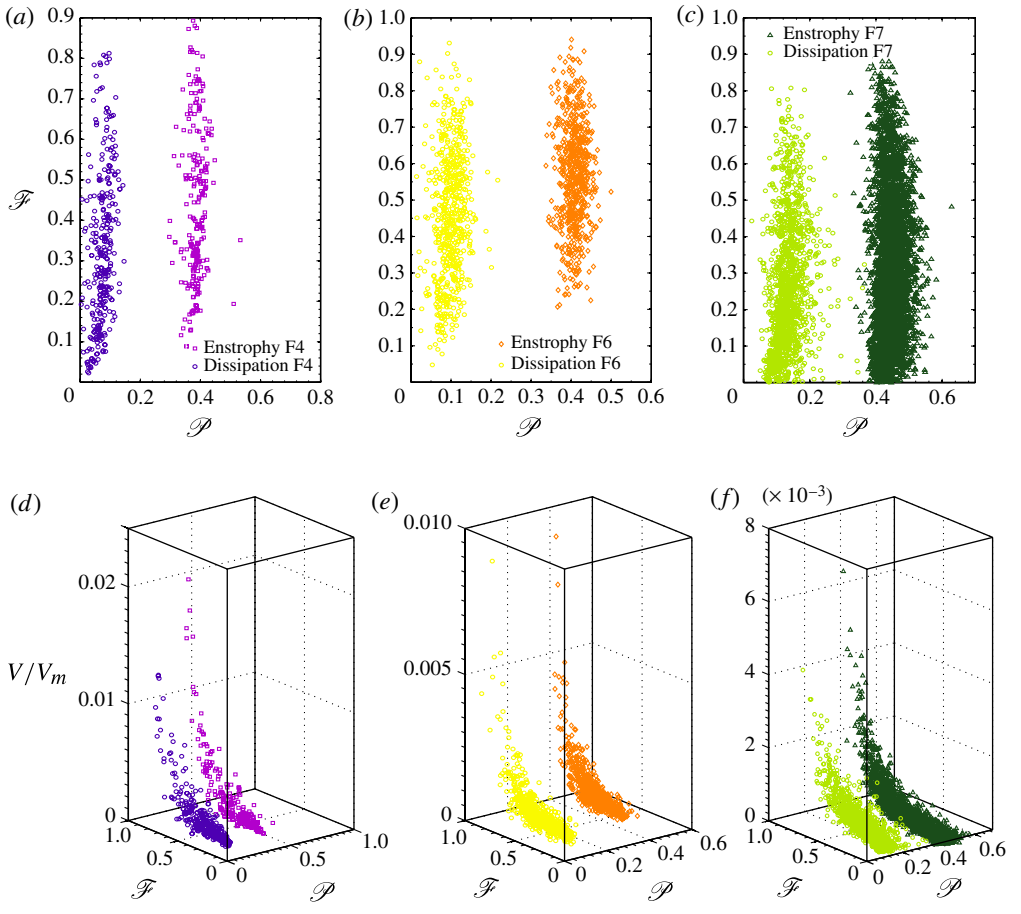

FIGURE 9. (Colour online) Comparison of shapefinders for enstrophy and dissipation structures filtered using F4, F6 and F7. Points for enstrophy structures are shifted by 0.3 on the $\mathscr{P}$-axis: (*a*,*d*) $L_4 = \lambda\ (24\eta)$; (*b*,*e*) $L_6 = 10\eta$; (*c*,*f*) $L_7 = 5\eta$.

The well-established view of vorticity aligning with the intermediate strain has been confirmed using the current DNS data. Recall that the present analysis is performed after 15 eddy turnover times in a decaying simulation when the turbulence is fully developed. The interaction between the strain and vorticity fields would require some time to develop before such preferential alignment could be firmly established. Ohkitani (2002) reported that in a decaying simulation such preferential alignment is established at a relatively early stage even before the maximum enstrophy is reached at ∼2 eddy turnover times, and it persists throughout the decaying period. The ratio of the most probable principal strain rates found in the current case is approximately −4:1:3. The total enstrophy production along each of the three principal strain directions is $\psi_1{:}\psi_2{:}\psi_3 = -1{:}1.41{:}2.06$, where $\psi_i = \lambda_i\,(\boldsymbol{\omega}\cdot\boldsymbol{e}_i)^2$ and $\boldsymbol{e}_i$ is the eigenvector of the principal strain rate λ_i. All these findings are consistent with previous studies.

In order to further examine whether vortices of various sizes undergo stretching, compression or a combination of both, enstrophy structures filtered at scale L_ω are considered. The typical alignment of this vorticity with the principal strains of the unfiltered strain field is shown in figure 11. For a large filter scale $L_\omega = 100\eta(0.50\ell)$,

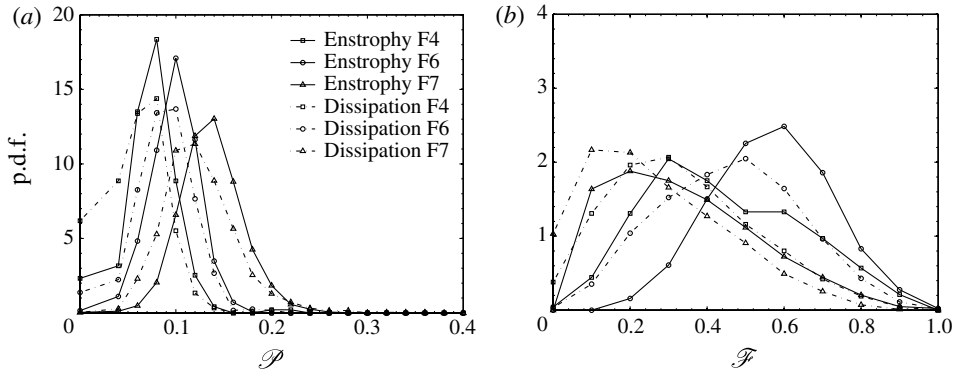

FIGURE 10. p.d.f. of (*a*) $\mathscr{P}$ and (*b*) $\mathscr{F}$ for enstrophy and dissipation structures considered for figure 9.

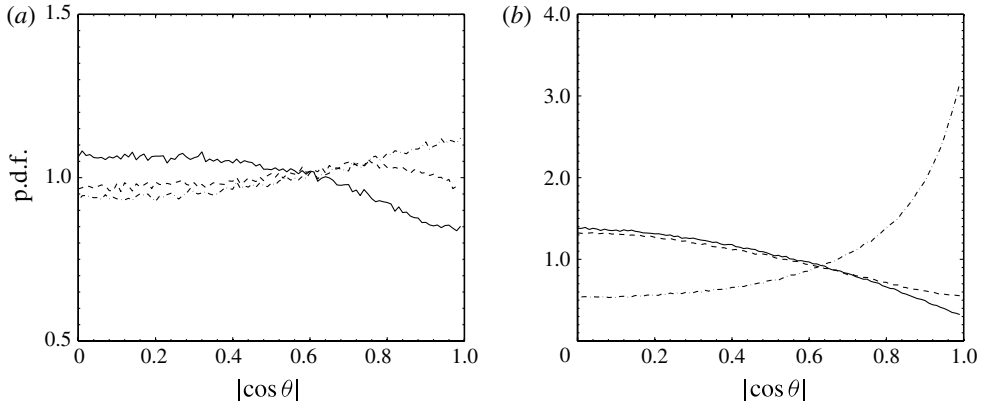

FIGURE 11. Typical p.d.f.s of alignment between vorticity filtered at scale L_ω and the principal directions of unfiltered strain field: (*a*) $L_\omega = 100\eta$, (*b*) $L_\omega = 15\eta$. Solid line λ_3, chain line λ_2 and dashed line λ_1.

there is no clear preferential alignment, suggesting the prevalence of random stretching or compression. The preferential alignment with the intermediate strain begins to appear at the filter setting $L_\omega = 50\eta(0.25\ell)$, and it becomes more evident as L_ω decreases further.

4.2. *Filtered strain field*

The local and non-local effects of strain on the vorticity have been noted in the past (Nomura & Post 1998; Hamlington *et al.* 2008). The total strain at a particular location $\boldsymbol{x}_0$ can be associated with the global vorticity field via the Biot-Savart law. Contributions to S_{ij} from the vorticity near $\boldsymbol{x}_0$ are termed 'local', while those which are from remote vorticity are termed 'non-local'. The alignment of vorticity with intermediate principal strain rate is observed to decrease when the local strain field induced by the vortex is eliminated (Hamlington *et al.* 2008).

In the light of these findings, the alignment between the filtered strain and vorticity fields is studied. From this point onwards, we shall denote the filter scale used on the

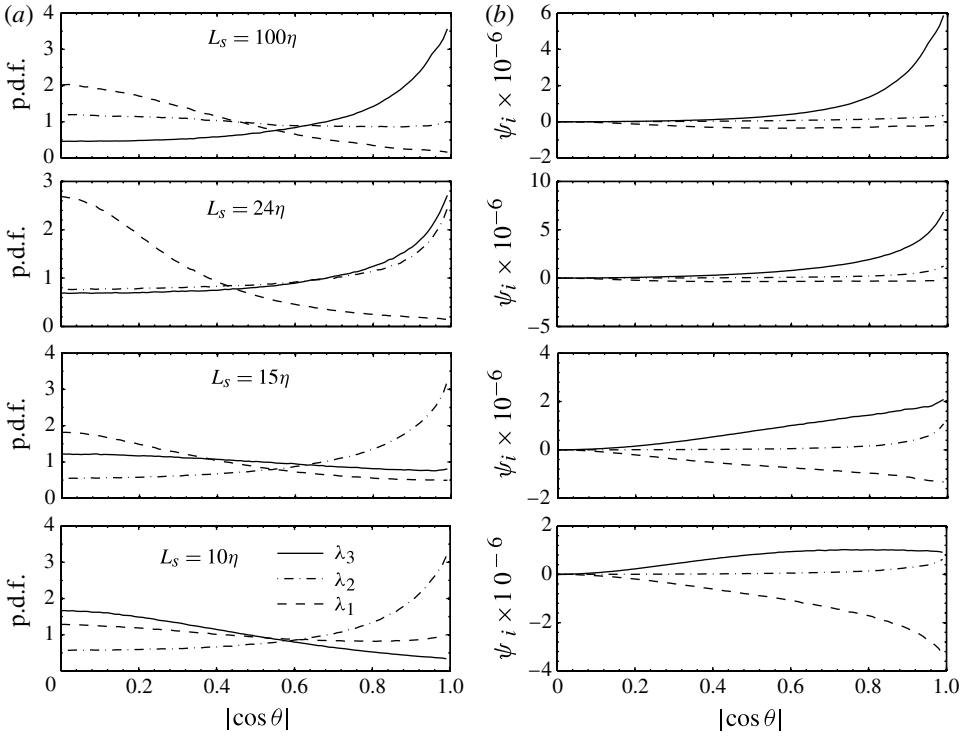

FIGURE 12. (*a*) p.d.f.s of alignment between vorticity filtered at scale $L_\omega = 15\eta$ and the principal directions of strain field filtered at different scales L_s given in the figures. The corresponding enstrophy generation is shown in (*b*). Solid line λ_3, chain line λ_2 and dashed line λ_1.

strain field and on the vorticity field as L_s and L_ω respectively. If the strain is filtered at a scale larger than that for the vorticity such that $L_s > L_\omega$, then the filtered strain field does not include the local contribution. Conversely if the strain field is filtered at a scale comparable to that of the vorticity field ($L_s \sim L_\omega$), then it represents primarily the local strain field induced by structures associated with the scale L_ω.

We focus on the small-scale vortices and two representative filter scales, $L_\omega = 15\eta$ and 10η, are considered for the vorticity field. The alignment p.d.f. for these two vorticity fields with the strain field filtered at scale L_s is shown in figures 12(*a*) and 13(*a*). In both cases, the filtered vorticity field aligns with the largest extensional strain λ_3 when the strain field is filtered at $L_s > L_\omega$, and the alignment p.d.f. for the intermediate strain λ_2 is rather flat. The contrast among results shown in figures 12 and 13 and those in figure 11 is strong. This suggests that the alignment statistics obtained with the total strain field, which includes the local self-induced strain, can completely mask the non-local effects. The filtered vorticity field only shows alignment with the intermediate strain when L_s approaches L_ω such that $L_s/L_\omega \lesssim 1.5$. The p.d.f. for the alignment of vorticity with either extensional strains, λ_2 and λ_3, is approximately the same as shown in figures 12 and 13 when $L_s/L_\omega \sim 1.5$. If the strain field is filtered at the same scale as, or smaller scale than, the vorticity field, a picture similar to that for unfiltered fields begin to emerge showing a predominant alignment between the vorticity and the intermediate strain.

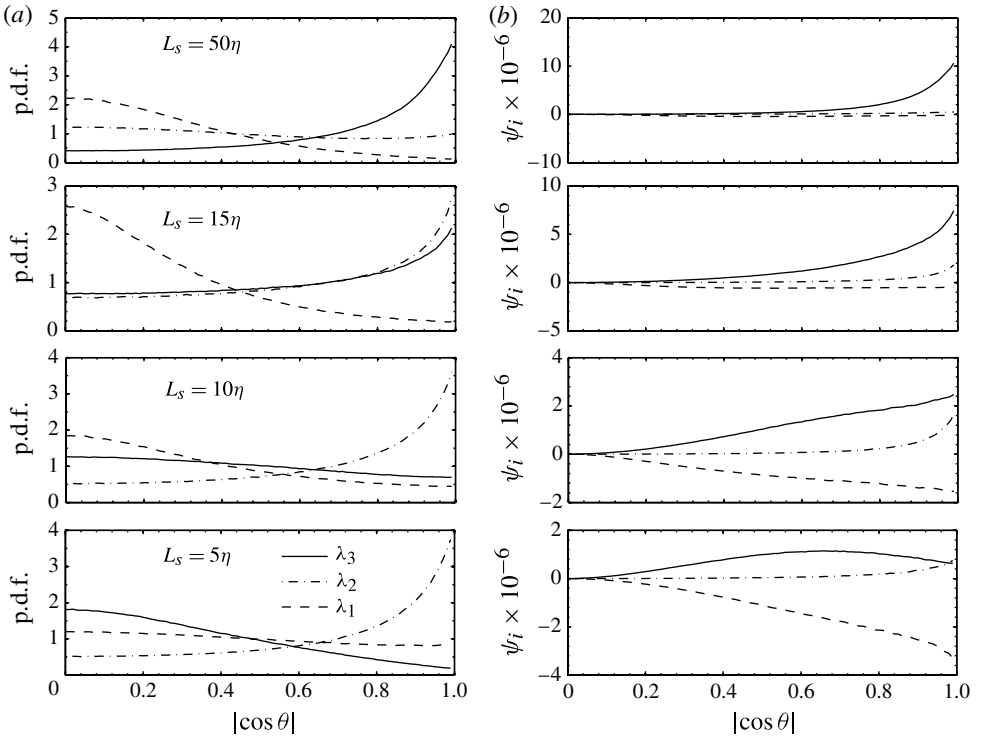

FIGURE 13. (*a*) p.d.f.s of alignment between vorticity filtered at scale $L_\omega = 10\eta$ and the principal directions of strain field filtered at different scales L_s given in the figures. The corresponding enstrophy generation is shown in (*b*). Solid line λ_3, chain line λ_2 and dashed line λ_1.

The gradual switching of the preferential alignment from the largest extensional strain to the intermediate strain can perhaps be understood from the solutions of the restricted Euler equations. Vieillefosse (1982) demonstrated that any flow would asymptotically align its vorticity with the positive intermediate strain if the dynamics of a single fluid particle is affected only by local effects in an inviscid and incompressible flow. It was shown by Nomura & Post (1998) that when the vorticity is misaligned with the strain field, the largest extensional strain would initially grow causing the principal axes to rotate such that the alignment with the intermediate strain is favoured.

The results of our study indicate that small-scale eddies are stretched predominantly by the largest principal strain originated from the strain field of larger eddies (i.e. the non-local strain field). This lends support to the view that axial vortex stretching is an important energy transfer mechanism. It is however obvious that when the scale separation is very large ($L_s \gg L_\omega$), the interaction between the two scales is minimal. This becomes evident when comparing the alignment between the strain field at $L_s = 150\eta$ and the vorticity field at $L_\omega = 15\eta$ and $L_\omega = 5\eta$ in figure 14. The former case, with a scale separation (L_s/L_ω) of 10, shows that the vorticity field filtered at $L_\omega = 15\eta$ is still largely aligned with the largest extensional strain of the large-scale strain field filtered at $L_s = 150\eta$. When the scale separation is increased to 30, the observed preferential alignment is greatly diminished.

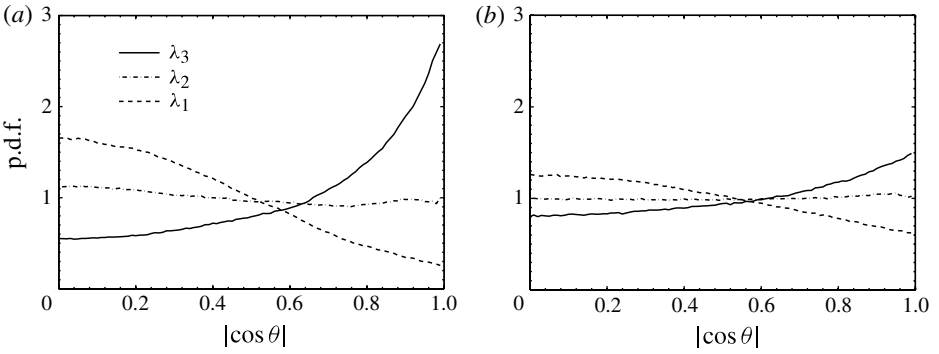

FIGURE 14. p.d.f. of alignment between filtered vorticity and strain fields at: (*a*) $L_s/L_\omega = 10$; and (*b*) $L_s/L_\omega = 30$.

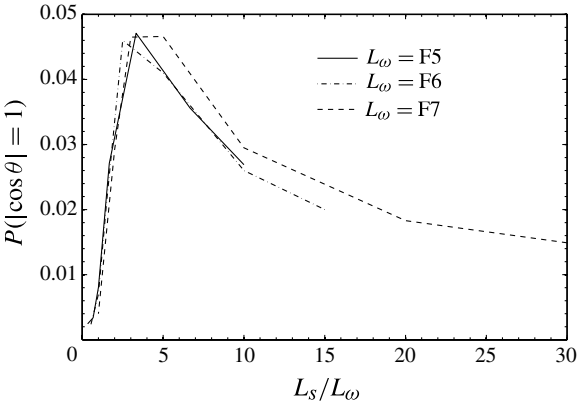

FIGURE 15. Probability of perfect alignment (i.e. $|\cos\theta| = 1$) for varying filter sizes for the strain field L_s and filtered vorticity field L_ω.

Figure 15 shows the probability, $P(0.99 < |\cos\theta| \leqslant 1)$, of obtaining a perfect alignment between the vorticity and the largest extensional strain for different filter scales. It can be seen that vorticity and strain fields are most perfectly aligned when $L_s/L_\omega \sim 3$–5. Thus the most significant axial stretching of small-scale eddies is due to the straining motion of eddies that are approximately 3–5 times larger. This is also apparent from examining the p.d.f. of $\cos\theta$ and enstrophy generation for various filter settings. The largest amount of enstrophy generation occurs when the structures are being stretched by the largest extensional strain induced by structures that are 3–5 times larger.

Examining figures 12(*b*) and 13(*b*), one finds that enstrophy is generated most significantly in the direction of the largest principal strain, λ_3. Most of the enstrophy generation occurs during stretching by the largest strain λ_3 due to non-local straining. This is evident especially when the alignment between $\boldsymbol{\omega}$ and λ_3 is the strongest, which occurs when $L_s/L_\omega \sim 3$–5. Although the intermediate strain remains mostly positive within the $\boldsymbol{\omega}^2$ structures, its role in generating enstrophy is less significant. These results strongly suggest that the worm-like structures are formed by axial

stretching rather than by the roll-up of vortex sheets suggested in a recent study (Bermejo-Moreno *et al.* 2009).

5. The spatial distribution of enstrophy structures

5.1. *Clustering*

Based on the visualizations, geometrical analyses and vorticity–strain field alignments, one can begin to form a conjecture on the spatial distribution of small-scale structures in relation to their larger counterparts. Small-scale tubular vortices are stretched axially by the strain field generated by eddies that are ∼3–5 times larger. Since the dissipation structures are fragmented and reside on the periphery of the enstrophy structures, smaller vortices on the periphery of the larger ones are likely to be intensified. The intermittent nature of small-scale vortices is quite apparent in figure 3. These worm-like structures are more concentrated around and in between the larger structures. As a result, they appear to be clustered in close proximity to larger structures rather than distributed randomly.

The small volume fraction occupied by fine-scale structures, as noted by Moisy & Jimenez (2004) and Worth (2010), highlights their intermittent nature and raises the question of whether they contribute significantly to the overall dynamics of the energy cascade. Moisy & Jimenez (2004) investigated small-scale clustering behaviour using the baricentres of individual structures. However, such an approach does not account for the spatial extent of structures as each one is represented by a point.

In the present work, volume fraction of the enstrophy structures at three filter scales, $L = \lambda$, 10η and 5η, within a sampling region $\mathscr{S}$ is considered instead. These three filter scales correspond to F4, F6 and F7 in table 1. The total domain can be divided into a number of cubic sampling regions $\mathscr{S}$, and the volume fraction $\mathscr{V} = V_s/V_L$ is computed within each $\mathscr{S}$, where V_s denotes the volume of the structures belonging to scale L found inside $\mathscr{S}$, and V_L denotes the volume of all the structures belonging to scale L in the entire domain. Sampling regions having $\mathscr{V}$ larger than a cut-off value are shown in figure 16. The sampling region size is $\mathscr{S} = (0.33\ell)^3$, and the cut-off values are 0.10 for F4, 0.08 for F6 and 0.06 for F7. Since the average volume fraction decreases with L as the fine structures occupy less volume, the cut-off value is also decreased with L. Figure 16 shows that structures are concentrated in certain regions of the domain. For example, there are nine distinct disconnected regions discernible for $L = \lambda$ shown in figure 16(*a*). The regions with large $\mathscr{V}$ for $L = \lambda$ and 10η are shown in figure 16(*b*) whereas the last frame of this figure includes such regions for all three filters. These regions overlap one another only partially, and the finer structures tend to spread out to fill up the spaces between neighbouring clusters of larger structures.

The p.d.f.s of $\mathscr{V}$ for four sizes of sampling regions, $\mathscr{S} = \ell^3$, $(0.50\ell)^3$, $(0.33\ell)^3$ and λ^3, are shown in figure 17 for F4, F6 and F7 structures. The mean of $\mathscr{V}$ for these three sets of filtered structures sampled over $\mathscr{S} = \ell^3$ is 0.0692, 0.0591 and 0.0458 respectively. The F7 structures occupy less volume and their narrower p.d.f. in figure 17(*a*) suggests that the variations in $\mathscr{V}$ for these structures is small. The increase in p.d.f. for $\mathscr{V} \geqslant 0.1$ and $\mathscr{V} \leqslant 0.02$ as $\mathscr{S}$ decreases suggests that the structures become more intermittent. For the F4 structures, a notable increase in the p.d.f. for $\mathscr{V} < 0.02$ occurs when $\mathscr{S} \leqslant (0.50\ell)^3$. The same occurs when $\mathscr{S} \leqslant (0.33\ell)^3$ for the other two filter scales, $L = 10\eta$ and 5η.

The above observations can provide insights into the clustering pattern of small-scale structures. A relatively small variation for $L = 5\eta$ suggests little clustering of the F7 structures within a region of size $\mathscr{S} = \ell^3$, while the broader p.d.f. for F4 and

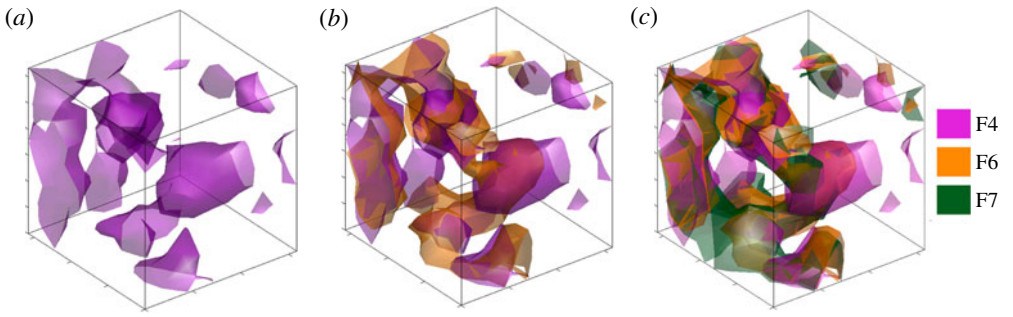

FIGURE 16. Regions, within the entire computational domain, containing high volume fraction of $\boldsymbol{\omega}^2$ structures educed at $L = \lambda$ (purple), 10η (orange) and 5η (green).

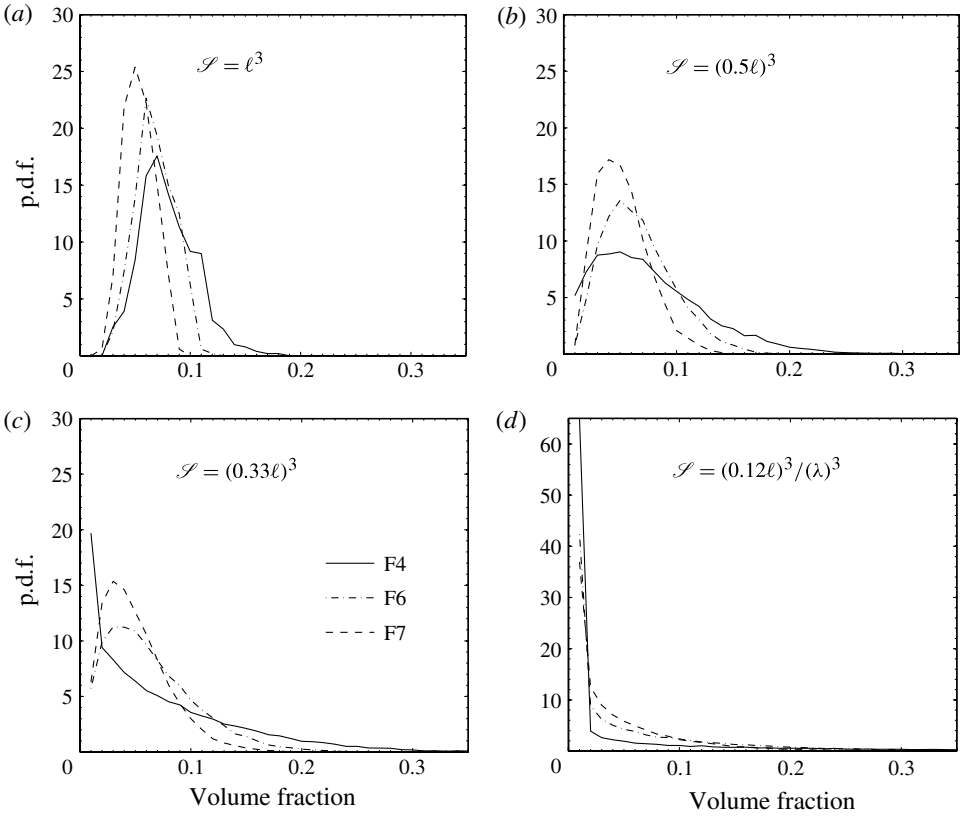

FIGURE 17. p.d.f. of volume fraction of $\boldsymbol{\omega}^2$ structures in different size of sampling region.

F6 suggests some clustering of these structures when $\mathscr{S} = \ell^3$. When increasing $\mathscr{S}$ to $(1.5\ell)^3$, the p.d.f. for the F4 structures becomes narrower, similar to the F7 case shown in figure 17(*a*). This implies little clustering of F4 (λ) structures within a region of size $\mathscr{S} = (1.5\ell)^3$.

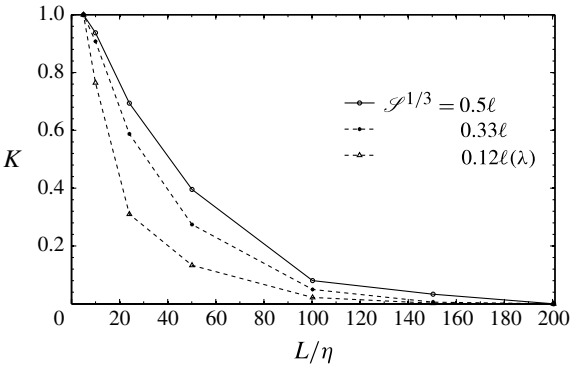

FIGURE 18. Spatial correlation between the volume fraction of $\boldsymbol{\omega^2}$ structures filtered at 5η and other scales L. Volume fraction is calculated for three different sampling regions.

The size of gaps between clusters of small-scale structures can be estimated. For $L = \lambda$, the probability of finding a nearly empty region, $\mathscr{V} \leqslant 0.02$, is zero when $\mathscr{S} = \ell^3$. Reducing $\mathscr{S}$ to $(0.5\ell)^3$ and $(0.33\ell)^3$ raises the probability to 12 % and 20 % respectively. This suggests that the clusters of λ-scale structures are separated by the nearly empty regions of size $\sim (0.5\ell)^3$. Very few nearly empty regions of size $(0.5\ell)^3$ can be found for finer structures at $L = 10\eta$ and 5η, but a significant number of such regions of size $\mathscr{S} = (0.33\ell)^3$ can be observed in figure 17(*c*). This suggests that these structures also form clusters, and they are separated by smaller gaps of the order of 0.33ℓ.

5.2. *Spatial correlation*

The spatial correlation of clusters at two different scales can be explored using the cross-correlation coefficient for $\mathscr{V}$ given by

$$K(L; L_1, \mathscr{S}) = \frac{\overline{\mathscr{V}'(L_1; \boldsymbol{x}, \mathscr{S})\mathscr{V}'(L; \boldsymbol{x}, \mathscr{S})}}{\mathscr{V}_{s,1}\mathscr{V}_s}, \tag{5.1}$$

where $\mathscr{V}'(L; \boldsymbol{x}, \mathscr{S}) = \mathscr{V}(L; \boldsymbol{x}, \mathscr{S}) - \mathscr{V}_m(L; \boldsymbol{x}, \mathscr{S})$, with the subscript m representing the mean value and the overbar indicating spatial averaging. The quantities $\mathscr{V}_{s,1}$ and $\mathscr{V}_s$ are the standard deviations of $\mathscr{V}(L_1; \boldsymbol{x}, \mathscr{S})$ and $\mathscr{V}(L; \boldsymbol{x}, \mathscr{S})$ respectively. It is clear that $K = 1$ when $L = L_1$. Its variation with L/η for $L_1 = 5\eta$ is shown in figure 18 for the three values of $\mathscr{S}$ considered in § 5.1.

The analysis of fine-scale clustering sizes and their gaps using K is followed here specifically to gain a global picture of the clustering arrangement over the entire domain. This is different from Bermejo-Moreno *et al.* (2009), who studied the local arrangement of individual structures and their closest neighbours using proximity analysis.

There is virtually no spatial correlation between structures at 5η and those at $L \geqslant 100\eta$ irrespective of the size of $\mathscr{S}$. The correlation coefficient increases as L decreases from 100η and the amount of increase in K depends on $\mathscr{S}$. For $\mathscr{S} = \lambda^3$, the spatial correlation between 5η and 10η structures is strong with $K = 0.76$. However, K drops to 0.31 when the 5η structures are correlated with $\lambda(24\eta)$ structures. This reduction in correlation decreases if $\mathscr{S}$ increases, which is because the spatial granularity of K decreases as $\mathscr{S}$ increases. A close examination of figure 18 clearly

shows that $K \leqslant 0.3$ when $L \simeq \mathscr{S}^{1/3}$. This suggests that the spatial correlation of the 5η structures becomes weaker with the structures having scales of $O(\mathscr{S}^{1/3})$. This is not surprising since the high value for K would indicate that the 5η structures are embedded within the larger ones, for example λ structures, but figure 3 shows the contrary. However, there appears to be some significant spatial correlation, $K \simeq 0.6$, between the λ and 5η structures within the sampling region of size $\mathscr{S} = (0.33\ell)^3$, which is $(2.7\lambda)^3$. Thus 5η structures can be found more frequently within a distance of 2.7λ from λ structures rather than overlapping them. As a word of caution, the result in figure 18 gives a qualitative insight into the clustering behaviour of fine-scale structures. Since this analysis has only been performed with a single snapshot of the DNS data, the above correlation is not meant to be a definitive correlation length between the clusters. If such a correlation length exists, it would be related to the degree of spatial intermittency and is likely to depend on Re_λ, which is not addressed in the present analysis.

The spatial correlation coefficient in figure 18 shows a marked increase for $L < 100\eta$ regardless of the sampling region size. In conjunction with our earlier results on the strong alignment of the vorticity field filtered at 5η with the largest principal strain filtered at λ to 15η discussed in § 4, a strong spatial correlation can be expected between enstrophy structures and those having dominant influence on stretching them. Therefore, the small-scale structures appear to cluster primarily around larger structures that are creating the strain field responsible for stretching them, and in the present study they are approximately 3–5 times larger.

6. Concluding remarks

A bandpass filtering procedure has been applied to a DNS dataset of homogeneous isotropic turbulence having $Re_\lambda = 141$ to educe enstrophy and dissipation structures of various scales. Applying the bandpass filter can effectively educe structures whose smallest characteristic length matches the chosen filter width, L. The filtered structures are visualized using a threshold value of $m_L + 1.5s_L$ for isosurfacing, where m and s are the mean and standard deviations of the respective fields filtered at scale L. A classical picture has emerged from this analysis showing that the educed structures become more worm-like as the filter scale L decreases. The small-scale structures are observed to concentrate around larger structures, which are mostly 'empty' rather than having smaller structures embedded within them. There is also a qualitative difference between the enstrophy and dissipation fields. The dissipation structures are more irregular in shape and are more fragmented, residing near the periphery of the enstrophy structures.

While a visual examination of the educed structures shows that there is a gradual change of structure morphology as L decreases, a more systematic and quantitative method to analyse the morphology of structures is introduced. This method is based on the Minkowski functionals, from which two dimensionless quantities called planarity $\mathscr{P}$ and filamentarity $\mathscr{F}$ are derived for a general shape description. Enstrophy structures obtained with $L = 100\eta$ are blob-like, characterized by low $\mathscr{P}$ and $\mathscr{F}$ values. They become increasingly tubular as suggested by an increase in $\mathscr{F}$ as L decreases from 50η to 10η. The planarity remains small for all L considered, suggesting that the enstrophy structures are mildly flattened and do not include any sheet-like structures for the turbulence considered in this study. This raises doubt on whether vortex sheets are indeed the precursors to the tubes. The increase in $\mathscr{F}$ as L decreases from 50η to 10η implies that finer structures are being stretched axially.

However, there is a high degree of variation in $\mathscr{F}$ and no distinctive characteristic length for these tubular structures can be found.

These observations lend support to the hypothesis that axial stretching of tubular structures acts as an energy transfer mechanism across eddies of different sizes. In particular, tubular vortices are found to be aligned with the maximum extensional strain generated by structures that are 3–5 times larger than themselves. The alignment of vorticity with the intermediate principal strain is only prominent when both of these fields are filtered at the same scale. These findings support the view that the strain field has both local and non-local contributions. Such effects cannot be easily deciphered by studying alignment characteristics in the unfiltered strain and vorticity fields. They also highlight the importance of the interaction between multiple scales. In short, we have found that the classical view of the energy cascade is qualitatively correct, with energy passing down the cascade as large vortices straining the smaller ones.

The enstrophy structures at 10η and 5η are found to be more concentrated near the periphery of the larger λ structures. Hence there is a spatial correlation between small-scale vortices and others that are slightly larger. There is virtually no spatial correlation between 5η and 100η structures, while the correlation between the 5η structures and those that are $\sim$3–5 times larger is pronounced. Since these dissipation-scale vortices are found to be stretched primarily by the strain field filtered at a scale that is 3–5 times larger, one might conclude that they cluster around those whose strain fields exert the most dominant effect on stretching them.

Acknowledgements

The financial support of Natural Sciences and Engineering Research Council of Canada is acknowledged. The help of Dr Tanahashi and Mr Shiwaku of Tokyo Institute of Technology in transferring the DNS data through an EPSRC project is gratefully acknowledged. Professor K. H. Moffatt is acknowledged for suggesting the Minkowski functionals.

Appendix. Examples of bandpass filtering

A simple illustration of bandpass filtering, using the Gaussian filter, is provided by an axisymmetric eddy of size ℓ in (r, θ, z) coordinates. The velocity field of this eddy is given by

$$\boldsymbol{u} = \Omega r \exp\left[\frac{-2(r^2+z^2)}{\ell^2}\right]\widehat{\boldsymbol{e}}_\theta, \tag{A 1}$$

where Ω is the characteristic angular velocity and $\widehat{\boldsymbol{e}}_\theta$ is the unit vector in the θ-direction. The bandpass filtered velocity field can be obtained using (2.5) and (2.6) as

$$\sqrt{L}\boldsymbol{u}_b^L = \frac{L^2\ell^5}{4h^7}\Omega r \exp\left[-\frac{r^2+z^2}{h^2}\right]\left\{5 - \frac{2(r^2+z^2)}{h^2}\right\}\widehat{\boldsymbol{e}}_\theta, \tag{A 2}$$

where

$$h^2 = L^2 + \frac{\ell^2}{2}. \tag{A 3}$$

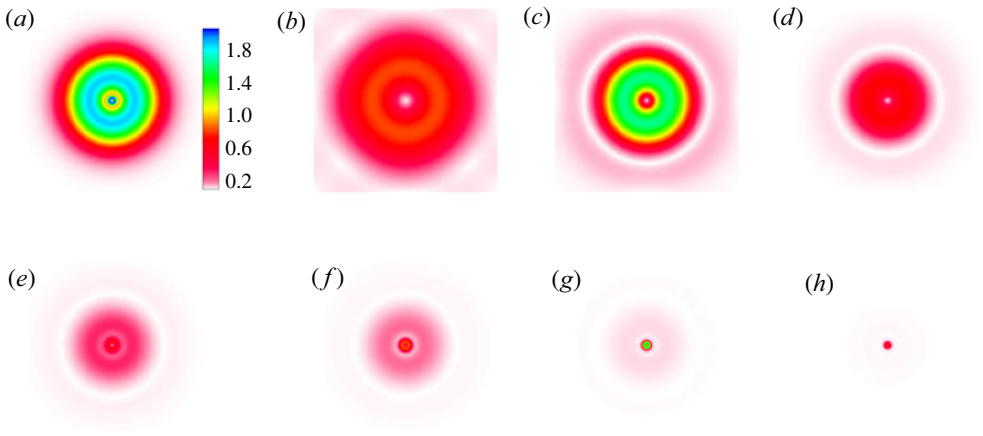

FIGURE 19. (Colour online) Plane cut (normal to the z-axis) of the unfiltered ,(a), and filtered velocity field, u_θ, for the superposition of two axisymmetric eddies of characteristic sizes ℓ_1 and ℓ_2. All filtered velocity fields shown are normalized to the same colour scaling as the unfiltered field: (a) $L = 1.2\ell_1$; (b) $L = \ell_1$; (c) $L = 0.5\ell_1$; (d) $L = 0.2\ell_1$; (e) $L = 1.2\ell_2$; (f) $L = \ell_2$; (g) $L = 0.5\ell_2$; (h) $L = 0.2\ell_2$.

It can be seen that eddies of sizes $L \gg \ell$ and $L \ll \ell$ are significantly attenuated:

$$\sqrt{L}|\boldsymbol{u}_b^L| \sim \left(\frac{\ell}{L}\right)^5 |\boldsymbol{u}| \quad \text{for } L \gg \ell \tag{A 4}$$

and

$$\sqrt{L}|\boldsymbol{u}_b^L| \sim \left(\frac{L}{\ell}\right)^2 |\boldsymbol{u}| \quad \text{for } L \ll \ell. \tag{A 5}$$

The effect of dilatation on the eddy is evident due to the change in the characteristic radius from ℓ to $\sqrt{2}h$. Eddies that are smaller than the filter width, L, can be suppressed quite effectively by the bandpass filter. However, the filter is less sharp for eddies with size larger than L. For a spherical eddy filtered at L, the resulting bandpass filtered field will predominantly contain traces of eddies with characteristic radii ranging from L to $4L$ with a maximum at $\ell = \sqrt{5}L$.

To further examine the effectiveness of this filter in a multi-scale situation, superposed axisymmetric eddies are considered as a second example. The two eddies have characteristic sizes of ℓ_1 and $\ell_2 = 0.1\ell_1$ with characteristic angular velocities of Ω_1 and $10\Omega_1$ respectively. The unfiltered original field is shown in figure 19(a), which clearly shows a stronger small eddy embedded in a weaker large eddy. It can be seen that the large eddy is most effectively extracted by setting $L = 0.5\ell_1$. Similarly, the small eddy can be clearly extracted by setting $L = 0.5\ell_2$, and the large eddy becomes negligible in the background.

Next consider a three-dimensional elliptical eddy of arbitrary aspect ratio with velocity field

$$\boldsymbol{u} = \Omega r \exp\left[-\frac{2r^2}{\ell_r^2} - \frac{2z^2}{\ell_z^2}\right] \widehat{\boldsymbol{e}}_\theta. \tag{A 6}$$

The bandpass filtered velocity field is readily shown to be

$$\sqrt{L}\boldsymbol{u}_b^L = \frac{L^2\ell_r^4\ell_z}{2h_r^4h_z}\Omega r\exp\left[-\frac{r^2}{h_r^2}-\frac{z^2}{h_z^2}\right]\left\{\frac{2-r^2/h_r^2}{h_r^2}+\frac{0.5-z^2/h_z^2}{h_z^2}\right\}\widehat{\boldsymbol{e}}_\theta, \tag{A 7}$$

where

$$h_r^2 = L^2+\frac{\ell_r^2}{2}\quad h_z^2 = L^2+\frac{\ell_z^2}{2}. \tag{A 8}$$

For a tubular eddy, $\ell_z \gg \ell_r$, the maximum $\sqrt{L}|\boldsymbol{u}_b^L|$ is obtained when $L = 0.5\ell_r$ and it falls off as $(\ell_r/L)^4$ for $L \gg \ell_r$ and $(L/\ell_r)^2$ for $L \ll \ell_r$. Moreover, for a pancake-like eddy with $\ell_r \gg \ell_z$, $\sqrt{L}|\boldsymbol{u}_b^L|$ has a maximum at $L = \ell_z$ and falls off as (ℓ_z/L) for $L \gg \ell_z$ and $(L/\ell_z)^2$ for $L \ll \ell_z$. Evidently, for vortices with more than one length scale, the filter predominantly educes structures whose smallest length scale matches that of the filter width L. The above analysis is obviously overly simplistic compared to the wide range of eddy shapes and sizes that are found in turbulent flows. Nevertheless, the examples demonstrate the effectiveness and shortcomings of the procedure used in this paper.

REFERENCES

ASHURST, WM. T., KERSTEIN, A. R., KERR, R. M. & GIBSON, C. H. 1987 Alignment of vorticity and scalar gradient with strain rate in simulated Navier–Stokes turbulence. *Phys. Fluids* **30**, 2343–2353.

BERMEJO-MORENO, I. & PULLIN, D. I. 2008 On the nonlocal geometry of turbulence. *J. Fluid Mech.* **603**, 101–135.

BERMEJO-MORENO, I., PULLIN, D. I. & HORIUTI, K. 2009 Geometry of enstrophy and dissipation, grid resolution effects and proximity issues in turbulence. *J. Fluid Mech.* **620**, 121–166.

BETCHOV, R. 1956 An inequality concerning the production of vorticity in isotropic turbulence. *J. Fluid Mech.* **1**, 497–504.

EINASTO, M., SAAR, E., LIIVAMÄGI, L. J., EINASTO, J., TAGO, E., MARTÍNEZ, V. J., STARCK, J.-L., MÜLLER, V., HEINÄMÄKI, P., NRMI, P., GRAMANN, M. & HÜTSI, G. 2007 The richest superclusters. i. Morphology. *Astron. Astrophys.* **476**, 697–711.

GOTO, S. 2008 A physical mechanism of the energy cascade in homogeneous isotropic turbulence. *J. Fluid Mech.* **605**, 355–366.

GOTO, S. & KIDA, S. 2003 A physical mechanism of the energy cascade in homogeneous isotropic turbulence. *Fluid Dyn. Res.* **33**, 403–431.

HADWIGER, H. 1957 *Vorlesungen über Inhalt, Oberfläache und Isoperimetrie*. Springer.

HAMLINGTON, P. E., SCHUMACHER, J. & DAHM, W. J. A. 2008 Local and nonlocal strain rate fields and vorticity alignmnet in turbulent flows. *Phys. Rev.* E **77**, 1–6.

HORIUTI, K. 2001 A classification method for vortex sheet and tube structures in turbulent flows. *Phys. Fluids* **13**, 3756–3774.

HORIUTI, K. & TAKAGI, Y. 2005 Identification method for vortex sheet structures in turbulent flows. *Phys. Fluids* **17**, 121703.

HOSOKAWA, I. & YAMAMOTO, K. 1990 Intermittency of dissipation in directly simulated fully developed turbulence. *J. Phys. Soc. Japan* **59**, 401404.

HUNT, J. C. R., WRAY, A. A. & MOIN, P. 1988 Eddies, stream, convergence zones in turbulent flows. *Tech. Rep.* CTR-S88. Center for Turbulence Research, Stanford, CA, USA.

JEONG, J. & HUSSAIN, F. 1995 On the identification of a vortex. *J. Fluid Mech.* **285**, 69–94.

JIMÉNEZ, J. 1992 Kinematic alignment effects in turbulent flows. *Phys. Fluids* A **4**, 652–654.

JIMÉNEZ, J. 1994 Columnar vortices in isotropic turbulence. *Meccanica* **29**, 453–464.

JIMÉNEZ, J. & WRAY, A. A. 1998 On the characteristics of vortex filaments in isotropic turbulence. *J. Fluid Mech.* **373**, 255–285.

JIMÉNEZ, J., WRAY, A. A., SAFFMAN, P. & ROGALLO, R. 1993 The structure of intense vorticity in isotropic turbulence. *J. Fluid Mech.* **255**, 65–90.

KERSCHER, M., SCHMALZING, J., RETZLAFF, J., BORGANI, S., BUCHERT, T., GOTTLÖBER, S., MÜLLER, V., PLIONIS, M. & WAGNER, H. 1997 Minkowski functionals of abell/aco clusters. *Mon. Not. R. Astron. Soc.* **284**, 73–84.

MECKE, K. R., BUCHERT, T. & WAGNER, H. 1994 Robust morphological measures for large-scales structures in the universe. *Astron. Astrophys.* **288**, 697–704.

MEYER, M., DESBRUN, M., SCHRODER, P. & BARR, A. H. 2002 Discrete differential-geometry operators for triangulared 2-manifolds. *Tech. Rep.* Caltech. http://www.multires.caltech.edu/pubs/difGeoOps.pdf.

MICHIELSEN, K. & RAEDT, H. DE 2001 Integral-geometry morphological image analysis. *Phys. Rep.* **347**, 461–538.

MOISY, F. & JIMENEZ, J. 2004 Geometry and clustering of intense structures in isotropic turbulence. *J. Fluid Mech.* **513**, 111–133.

NOMURA, K. K. & POST, G. K. 1998 The structure and dynamics of vorticity and rate of strain in incompressible homogeneous turbulence. *J. Fluid Mech.* **377**, 65–97.

OHKITANI, K. 2002 Numerial study of comparison of vorticity and passive vectors in turbulence and inviscid flows. *Phys. Rev.* E **65**, 046304.

PASSOT, T., POLITANO, H., SULEM, P. L., ANGILELLA, J. R. & MENEGUZZI, M. 1995 Instability of strained vortex layers and vortex tube formation in homogeneous turbulence. *J. Fluid Mech.* **282**, 313–338.

RUETSCH, G. R. & MAXEY, M. R. 1994 Small-scale features of vorticity and passive scalar fields in homogeneous isotropic turbulence. *Phys. Fluids* A **3**, 1587–1597.

SAHNI, V., SATHYAPRAKASH, B. S. & SHANDARIN, S. F. 1998 Shapefinders: a new shap diagnostic for large-scale structure. *Astrophys. J.* **495**, L5–L8.

SCHMALZING, J. & BUCHERT, T. 1997 Beyond genus statistics: a unifying approach to the morphology of cosmic structure. *Astrophys. J.* **482**, L1–L4.

SCHMALZING, J., BUCHERT, T., MELOTT, A. L., SAHNI, V., SATHYAPRAKASH, B. S. & SHANDARIN, S. F. 1999 Disentangling the cosmic web I. Morphology of isodensity contours. *Astrophys. J.* **526**, 568–578.

SHANDARIN, S. F., SHETH, J. V. & SAHNI, V. 2004 Morphology of the supercluster-void network in $\wedge$cdm cosmology. *Mon. Not. R. Astron. Soc.* **353**, 162–178.

SHE, Z.-S., JACKSON, E. & ORSZAG, S. A. 1991 Structure and dynamics of homogeneous turbulence: models and simulations. *Proc. R. Soc. Lond.* A **434**, 101–124.

SHETH, J. V. & SAHNI, V. 2005 Exploring the geometry topology and morpholgy of large scale structure using Minkowski functionals. *Curr. Sci.* **1101–1116**, 568–578.

SHETH, J. V., SHANDARIN, S. F. & SATHYAPRAKASH, B. S. 2003 Measuring the geometry and topology of large-scale structure using SURFGEN: methodology and preliminary results. *Mon. Not. R. Astron. Soc.* **343**, 22–46.

SIGGIA, E. D. 1981 Numerical study of small-scale intermittency in three-dimensional turbulence. *J. Fluid Mech.* **107**, 375–406.

TANAHASHI, M., MIYAUCHI, M. & IKEDA, J. 1999 Fine scale structure in turbulence, fluid mechanics and its application. In *Simulation and Identification of Organized Structures in Flows, Fluid Mechanics and its Applications. IUTAM Symposium,* vol. 52, pp. 131–140. IUTAM.

TENNEKES, A. A. 1968 Simple model for the small-scale structure of turbulence. *Phys. Fluids* **11**, 669–670.

THOMPSON, A. C. 1996 *Minkowski Geometry*. Cambridge University Press.

TOWNSEND, A. A. 1951 On the fine-scale structure of turbulence. *Proc. R. Soc. Lond.* A **208**, 534–542.

VIEILLEFOSSE, P. 1982 Local interaction between vorticity and shear in a perfect incompressible fluid. *J. Phys. Paris* **43**, 837–842.

VINCENT, A. & MENEGUZZI, M. 1991 The spatial structure and statistical properties of homogeneous turbulence. *J. Fluid Mech.* **225**, 1–20.

VINCENT, A. & MENEGUZZI, M. 1994 The dynamics of vorticity tubes in homogeneous turbulence. *J. Fluid Mech.* **258**, 245–254.

WILKIN, S. L., BARENGHI, C. F. & SHUKUROV, A. 2007 Magnetic structures produced by the small-scale dynamo. *Phys. Rev. Lett.* **99**, 134501.

WORTH, N. 2010 Tomographic-PIV measurement of coherent dissipation scale structures. PhD thesis, University of Cambridge, Cambridge.

YANG, Y. & PULLIN, D. I. 2011 Geometric study of Lagrangian and Eulerian structures in turbulent channel flow. *J. Fluid Mech.* **674**, 67–92.

YANG, Y., PULLIN, D. I. & BERMEJO-MORENO, I. 2010 Multi-scale geometrical analysis of Lagrangian structures in isotropic turbulence. *J. Fluid Mech.* **654**, 233–270.